

Surface Methods for the Computation of Realistic Symplectic Transfer Maps from Numerical Field Data on a Grid

Alex Dragt

January 16, 2017

Abstract

The passage of a charged particle through the field \mathbf{B} of a magnetic element may be described by a symplectic transfer map \mathcal{M} . This map is generated by the Hamiltonian H specifying charged-particle motion. \mathcal{M} may be written as a product of Lie transformations, and the generators for these transformations can be found by integrating a set of differential equations whose driving terms are the Taylor coefficients arising in the Taylor expansion of H about a design orbit. The Hamiltonian formulation of charged particle motion, required to exploit symplectic structure, involves the use of a vector potential \mathbf{A} . Therefore expanding H in a Taylor series requires a Taylor expansion of \mathbf{A} . For realistic elements \mathbf{B} is known (using codes such as those available from *Vector Fields*) only on a three-dimensional grid. The challenge is to reliably compute high-order Taylor coefficients for \mathbf{A} based on this grid data.

At first sight this appears to be an impossible task. Numerical differentiation of grid data is well known to be very sensitive to numerical noise: numerical differentiation amplifies noise. And high derivatives are required to compute \mathcal{M} to high order. This problem can be overcome by employing surface methods which involve the use of inverse Laplacian kernels. Such kernels are smoothing, and this smoothing overcomes the noise associated with numerical differentiation. Moreover, the Maxwell equations are satisfied exactly, and analyticity is assured.

One final point is that the optimal termination of fringe fields requires the use of a gauge at element ends for which \mathbf{A} is as small as possible. This *minimum* gauge is found to be the Poincaré-Coulomb gauge.

In summary, with the use of surface methods, and the use of the minimum gauge at element ends, it is now possible for the first time to compute realistic symplectic transfer maps to high order including all multipole-error and fringe-field effects. These maps can then be used to realistically predict/evaluate the expected performance of both linear and circular machines.

1 Lie Algebraic Preliminaries

1.1 Poisson Brackets

Let the symbol z denote the collection of canonical phase-space variables

$$z = (z_1, z_2, \dots, z_{2n}) = (q_1, \dots, q_n; p_1, \dots, p_n). \quad (1.1)$$

Let $f(z, t)$ and $g(z, t)$ be any two (possibly time-dependent) functions of z . Define their *Poisson bracket* $[f, g]$ by the rule

$$[f, g] = \sum_j (\partial f / \partial q_j)(\partial g / \partial p_j) - (\partial f / \partial p_j)(\partial g / \partial q_j). \quad (1.2)$$

By this definition there are the *fundamental* Poisson brackets

$$[z_a, z_b] = J_{ab} \quad (1.3)$$

where J is the $2n \times 2n$ matrix

$$J = \begin{pmatrix} 0 & I \\ -I & 0 \end{pmatrix}. \quad (1.4)$$

Here $2n$ is the phase-space dimension, and 0 and I denote $n \times n$ zero and identity blocks, respectively. The matrix J is sometimes called the *Poisson matrix*.

Evidently Poisson brackets have the *antisymmetry* property

$$[g, f] = -[f, g]. \quad (1.5)$$

It can be verified that Poisson brackets also satisfy the *Jacobi identity*. Let f , g , and h be any three phase-space functions. Then there is the identity

$$[f, [g, h]] + [g, [h, f]] + [h, [f, g]] = 0. \quad (1.6)$$

Consequently, the Poisson bracket satisfies the requirements for a *Lie product*. The set of all phase-space functions forms a Lie algebra with the Poisson bracket being the Lie product.

1.2 Lie Operators and Lie Transformations

Given any function $f(z, t)$, define an associated *differential operator*, denoted by $:f:$ and called a *Lie operator*, by the rule

$$:f := \sum_j (\partial f / \partial q_j)(\partial / \partial p_j) - (\partial f / \partial p_j)(\partial / \partial q_j). \quad (1.7)$$

Then, if $g(z, t)$ is any other function, the action of $: f :$ on g is defined by writing

$$: f : g = \sum_j (\partial f / \partial q_j) (\partial g / \partial p_j) - (\partial f / \partial p_j) (\partial g / \partial q_j) = [f, g]. \quad (1.8)$$

Thus, a Lie operator may be viewed as a Poisson bracket waiting to happen.

In general Lie operators do not commute. However, the commutator $\{ : f :, : g : \}$ of any two Lie operators $: f :$ and $: g :$ is again a Lie operator. Indeed, as a consequence of the Jacobi identity, the commutator $\{ : f :, : g : \}$ is given in terms of the Poisson bracket of the two underlying functions f and g by the relation

$$\{ : f :, : g : \} = : f : : g : - : g : : f : = [f, g] : . \quad (1.9)$$

The relation (1.8) defines the action of $: f :$. Powers of $: f :$ can be defined by the rules

$$: f :^0 g = g, \quad (1.10)$$

$$: f :^2 g = [f, [f, g]], \text{ etc.} \quad (1.11)$$

Now that powers of $: f :$ have been defined, power series in $: f :$ can also be defined. Of particular interest is the power series associated with the exponential function by the rule

$$\exp(: f :) = e^{(: f :)} = \sum_{m=0}^{\infty} : f :^m / m!. \quad (1.12)$$

The operator $\exp(: f :)$, called a *Lie transformation*, has the action

$$\exp(: f :)g = g + [f, g] + (1/2!)[f, [f, g]] + \dots \quad (1.13)$$

In this context, $: f :$ is called a *Lie generator*.

1.3 Symplectic Transfer Maps

Let z^{in} denote the *initial* condition for a particle as it enters a beam-line or collection of beam-line elements, and let z^{fin} denote the *final* condition upon exit. The initial and final conditions will be related by a *transfer map* \mathcal{M} , and we express this relation by writing

$$z^{\text{fin}} = \mathcal{M}z^{\text{in}}. \quad (1.14)$$

Suppose a small change dz^{in} is made in the initial condition. The result will be an associated small change dz^{fin} in the final condition. These small changes will be connected by the relation

$$dz^{\text{fin}} = Mdz^{\text{in}} \quad (1.15)$$

where M is the Jacobian matrix

$$M_{ab} = \partial z_a^{\text{fin}} / \partial z_b^{\text{in}}. \quad (1.16)$$

It can be shown that if \mathcal{M} is the result of integrating Hamilton's equations of motion, then its associated Jacobian matrix M will satisfy the condition

$$M^T J M = J. \quad (1.17)$$

Here M^T denotes the transpose of M . A matrix that satisfies (1.17) is said to be *symplectic*; correspondingly \mathcal{M} is called a *symplectic map*. Note that in general M depends on z^{in} . However, J does not. Therefore (1.17), since it must hold for all z^{in} , places strong (nonlinear) restrictions on \mathcal{M} .

1.4 Representation of Symplectic Transfer Maps

1.4.1 Taylor Representation

Suppose \mathcal{M} has the property that it maps the origin into itself. That is, we assume that there is a Taylor expansion of the form

$$z_a^{\text{fin}} = \sum_b R_{ab} z_b^{\text{in}} + \sum_{bc} T_{abc} z_b^{\text{in}} z_c^{\text{in}} + \sum_{bcd} U_{abcd} z_b^{\text{in}} z_c^{\text{in}} z_d^{\text{in}} + \dots. \quad (1.18)$$

This can always be accomplished by the use of *deviation* variables. If \mathcal{M} is symplectic, then R must be a symplectic matrix. Moreover, the Taylor coefficients T, U, \dots cannot be arbitrary, but are constrained by complicated nonlinear relations that follow from the symplectic condition (1.17). Finally, in general the series (1.18) cannot be truncated without violating the symplectic condition.

1.4.2 Factored Lie Product Representation

However, it can be shown that \mathcal{M} can also be written in the Lie product form

$$\mathcal{M} = \mathcal{R} \exp(: f_3 :) \exp(: f_4 :) \dots \quad (1.19)$$

where \mathcal{R} is the linear symplectic map associated with R , and the f_m are *homogeneous* polynomials of degree m . Unlike the Taylor coefficients, there are no restrictions on the f_m imposed by the symplectic condition. Any symplectic map is uniquely specified by a symplectic matrix and a collection of homogeneous polynomials that describe the nonlinear part of the map, and conversely. Also, the product (1.19) can be truncated at any stage without violating the symplectic condition. It can be shown that each factor in (1.19) is a symplectic map, and the product of any number of symplectic maps is also a symplectic map.

1.5 Concatenation (Multiplication) of Symplectic Maps

Suppose \mathcal{M}_f and \mathcal{M}_g are two symplectic maps written in the factorized product forms

$$\mathcal{M}_f = \mathcal{R}_f \exp(: f_3 :) \exp(: f_4 :) \cdots , \quad (1.20)$$

$$\mathcal{M}_g = \mathcal{R}_g \exp(: g_3 :) \exp(: g_4 :) \cdots , \quad (1.21)$$

and we wish to find their product \mathcal{M}_h , also written in the factorized form

$$\mathcal{M}_f \mathcal{M}_g = \mathcal{M}_h = \mathcal{R}_h \exp(: h_3 :) \exp(: h_4 :) \cdots . \quad (1.22)$$

For example, \mathcal{M}_f and \mathcal{M}_g might be the maps for two successive sections f and g of a beam line, and \mathcal{M}_h would then be the map for the beam line consisting of the section f followed by the section g .

There are standard Lie-algebraic rules, called the *Baker-Campbell-Hausdorff formula*, for the manipulation of noncommuting exponents. Using these rules gives, in this context, the results

$$R^h = R^g R^f , \quad (1.23)$$

$$h_3 = f_3^{tr} + g_3 , \quad (1.24)$$

$$h_4 = f_4^{tr} + g_4 + [f_3^{tr}, g_3]/2. \quad (1.25)$$

$$h_5 = f_5^{tr} + g_5 - [g_3, f_4^{tr}] + \frac{1}{3} : g_3 :^2 f_3^{tr} - \frac{1}{6} : f_3^{tr} :^2 g_3, \text{ etc.} \quad (1.26)$$

Results of this kind are currently available through h_8 . Here the f_m^{tr} , where tr denotes *transformed*, are defined by the rule

$$f_m^{tr}(z) = f_m[(R^g)^{-1}z]. \quad (1.27)$$

1.6 Map Inversion

The map \mathcal{M} given in the factorized product form (1.19) is said to be in *forward* factorized form. Its inverse can be written as

$$\mathcal{M}^{-1} = \cdots \exp(- : f_4 :) \exp(- : f_3 :) \mathcal{R}^{-1} \quad (1.28)$$

where the matrix associated with \mathcal{R}^{-1} is R^{-1} . This *reversed* factorized product form can be brought to the standard forward factorized form using the concatenation formulas of Section 1.5.

1.7 Computation of \mathcal{M}

Let $H(z, t)$ be the Hamiltonian that gives rise to \mathcal{M} . In this subsection we will sketch how \mathcal{M} can be computed in terms of H . In particular, we will describe how the R and the f_m appearing in (1.19) can be computed in terms of the components of H .

If deviation variables are employed, $H(z, t)$ will have an expansion of the form

$$H = \sum_{m=2}^{\infty} H_m(z, t) \quad (1.29)$$

where the H_m are homogeneous polynomials of degree m in the variables z .

For computational simplicity we will first choose to write \mathcal{M} in the reversed factorized product form

$$\mathcal{M} = \cdots \exp(: \bar{f}_4 :) \exp(: \bar{f}_3 :) \mathcal{R}. \quad (1.30)$$

Results in the standard factorized form (1.19) can then be found from (1.30) using the concatenation formulas of Section 1.5. Here, as the notation is intended to suggest, the \mathcal{R} appearing in (1.19) turns out to be the same as the \mathcal{R} appearing in (1.30), and \mathcal{R} is a linear map whose action is described by a symplectic matrix R . However, the f_m are different from the \bar{f}_m , and use of the concatenation formulas is required to find the f_m once the \bar{f}_m have been found.

In Lie-algebraic language, it can be shown that \mathcal{M} obeys the equation of motion

$$\dot{\mathcal{M}} = \mathcal{M} : -H : \quad (1.31)$$

with the initial condition

$$\mathcal{M}(t^{\text{in}}) = \mathcal{I}. \quad (1.32)$$

Insertion of the Ansatz (1.30) for \mathcal{M} into the equation of motion (1.31), and employing the decomposition (1.29) for H , yields equations of motion for R and the \bar{f}_m .

1.7.1 Computation of R

We begin with the computation of R . Suppose the *symmetric* matrix S is defined by writing H_2 in the form

$$H_2(z, t) = (1/2) \sum_{ab} S_{ab}(t) z_a z_b. \quad (1.33)$$

Then it can be shown that R obeys the matrix differential equation

$$\dot{R} = JSR \quad (1.34)$$

with the initial condition

$$R(t^{\text{in}}) = I. \quad (1.35)$$

We see that $R(t)$ is determined by the quadratic part of the Hamiltonian. Finally, it can be shown that $R(t)$, the solution to (1.34) with the initial condition (1.35) for any symmetric matrix $S(t)$, is a symplectic matrix.

1.7.2 Computation of the \bar{f}_m

We next turn to the computation of the \bar{f}_m from which the f_m can ultimately be found. Given the Hamiltonian pieces $H_m(z, t)$ with $m > 2$, define *interaction picture* Hamiltonian pieces $H_m^{\text{int}}(z, t)$ by the rule

$$H_m^{\text{int}}(z, t) = H_m(Rz, t). \quad (1.36)$$

Note that in general $H_m^{\text{int}}(z, t)$ will be “time dependent” even if H_m is not because R is time dependent.¹

With this background in mind, it can be shown that the \bar{f}_m obey the differential equations

$$\dot{\bar{f}}_3 = -H_3^{\text{int}}, \quad (1.37)$$

$$\dot{\bar{f}}_4 = -H_4^{\text{int}} + (: \bar{f}_3 : / 2)(-H_3^{\text{int}}), \quad (1.38)$$

$$\dot{\bar{f}}_5 = -H_5^{\text{int}} + : \bar{f}_3 : (-H_4^{\text{int}}) + (1/3) : \bar{f}_3 :^2 (-H_3^{\text{int}}), \text{ etc}, \quad (1.39)$$

with the initial conditions

$$\bar{f}_m(t^{\text{in}}) = 0. \quad (1.40)$$

Results of this kind are currently available through \bar{f}_8 .

2 Specification of H and the Use of Surface Methods

For Accelerator Physics applications it is often convenient to take the Cartesian z coordinate to be the *independent* variable and to treat time as a *dependent* variable. When this is done, a Hamiltonian formulation is still possible. Let X and Y be suitably scaled spatially transverse deviation variables, and let P_x and P_y be suitably scaled canonically conjugate deviation momenta. Also, let τ be a suitably scaled time deviation variable. Its canonically conjugate momentum P_τ will then be the negative of a suitably scaled energy deviation variable. For simplicity let us also assume that the magnetic field \mathbf{B} is static and that there is no electric field.

In this case the equations of motion for the deviation variables $(X, Y, \tau, P_x, P_y, P_\tau)$, all of which have been scaled to be dimensionless, are governed by the Hamiltonian H given by the rule

$$\begin{aligned} H(X, Y, \tau, P_x, P_y, P_\tau; z) = \\ - (1/\ell) \{ [1 - (2P_\tau/\beta_0) + P_\tau^2 - (P_x - A_x^s)^2 - (P_y - A_y^s)^2]^{1/2} + A_z^s + (P_\tau/\beta_0) - 1 \}. \end{aligned} \quad (2.1)$$

¹In Section 2 we will see that in the case of Accelerator Physics a coordinate often plays the role of the independent variable, and therefore the H_m themselves, particularly in fringe-field regions, generally depend on the independent variable.

Here ℓ is a scale length, β_0 is the relativistic β factor for the design orbit, and $A_x^s \dots$ are the components of a suitably scaled dimensionless vector potential \mathbf{A}^s .

According to (1.29), we must expand H as a sum of homogeneous polynomials. But now we see that in general there is problem when one desires to use realistic field data. Expansion of H to high order requires knowledge, to high order, of the X, Y Taylor coefficients for \mathbf{A}^s about the design orbit. But all we know for realistic fields, particularly for the case of iron dominated magnets, are the values of \mathbf{B} on a grid as provided by numerical field solvers. And, as outlined in the Abstract, numerical differentiation of grid data is well known to be very sensitive to numerical noise: differentiation amplifies noise.

In the next two sections we will describe how this problem can be overcome by employing surface methods which involve, in effect, the use of inverse Laplacian kernels. Such kernels are smoothing, and this smoothing overcomes the noise associated with numerical differentiation. Moreover, we will see that the Maxwell equations are satisfied exactly.

But first let us make an initial observation. Suppose V is some simply connected volume bounded by a surface S . Assume also that \mathbf{B} is source free (divergence and curl free) in V . Finally, assume that on S the quantity B_n , the normal component of \mathbf{B} , is specified. Then this information is sufficient to specify \mathbf{B} everywhere in V .

Why is this so? Since \mathbf{B} is assumed curl free in V , within V there must be a potential ψ such that

$$\mathbf{B} = \nabla\psi. \quad (2.2)$$

And, since \mathbf{B} is divergence free, within V the potential ψ must be *harmonic*,

$$\nabla^2\psi = 0. \quad (2.3)$$

Now it follows from (2.2) that on S there must be the relation

$$\mathbf{n} \cdot \nabla\psi = \mathbf{n} \cdot \mathbf{B} = B_n. \quad (2.4)$$

Here \mathbf{n} is the outward unit normal on S . Taken together (2.3), with the boundary condition (2.4), comprise the *Neumann problem* for ψ . It is known to have a unique solution specifying ψ within V up to a constant. Thus, by (2.2), specification of B_n on S completely determines \mathbf{B} within V . There is, however, one caveat: a consistency condition must be imposed on the boundary data B_n . Since \mathbf{B} is divergence free in V , there must be the result

$$0 = \int_V d^3\mathbf{r} \nabla \cdot \mathbf{B} = \int_S \mathbf{B} \cdot d\mathbf{S}' = \int_S dS' B_n, \quad (2.5)$$

the integral of B_n over the surface S must vanish.

3 Surface Methods for Straight Beam-Line Elements

We have seen, at the end of Section 2, that in principle a knowledge of the normal component of \mathbf{B} on a bounding surface S determines \mathbf{B} within the bounded volume V . In practice

however, explicit calculations of this kind are difficult to implement for general volumes V . Fortunately, there are two cases for which such calculations are feasible; and these cases are applicable to straight beam line elements, which include solenoids, quadrupoles, sextuples, etc., and small-amplitude wigglers. These are the cases where S is a cylinder with circular or elliptical cross section. Figure 1 illustrates the use of a circular cylinder, and Figure 2 illustrates the use of an elliptical cylinder. The circular cylinder is appropriate for solenoids, quadrupoles, sextuples, etc. While more complicated because of its employment of *Mathieu* functions, the use of elliptical cylinders is advantageous for the case of wigglers with small gaps and wide pole faces.

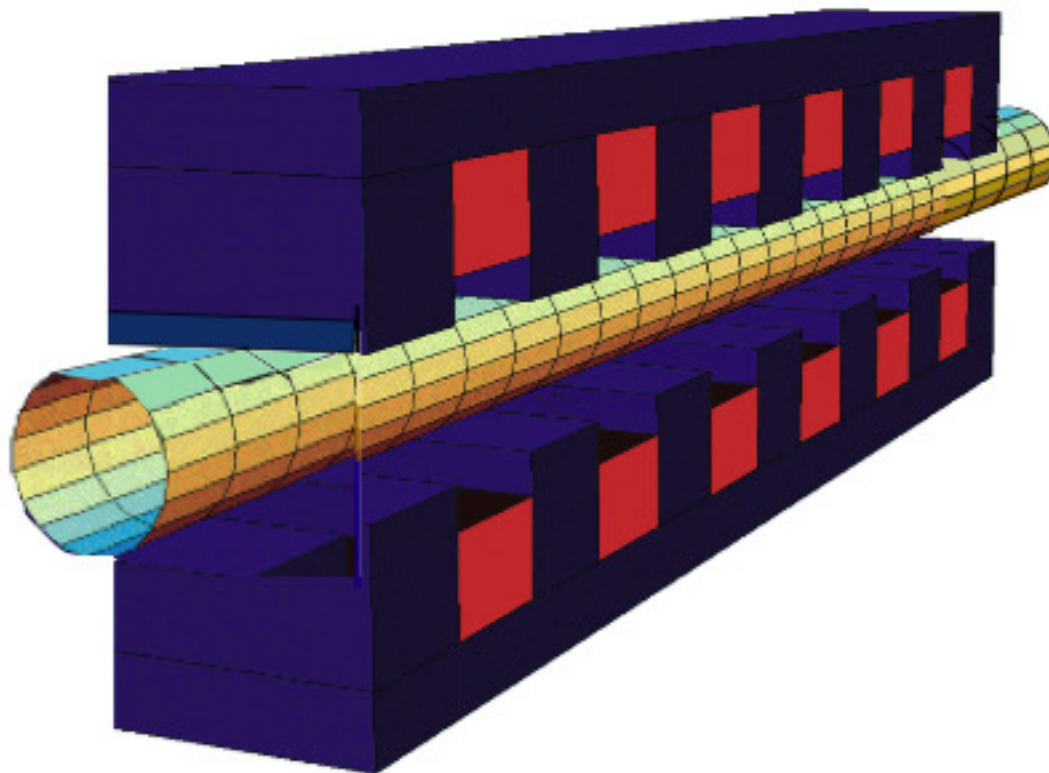


Figure 1: A circular cylinder of radius R , centered on the z -axis, fitting within the bore of a beam-line element, in this case a wiggler, and extending beyond the fringe-field regions at the ends of the beam-line element.

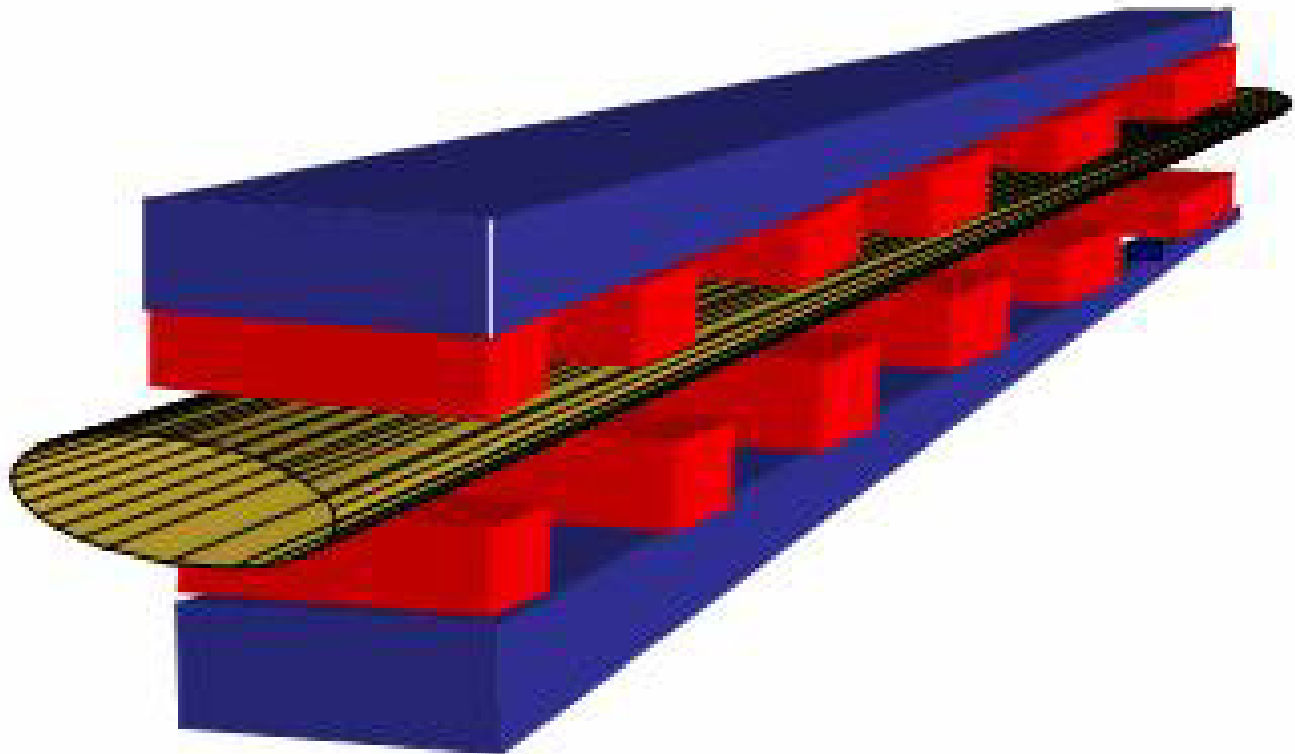


Figure 2: An elliptical cylinder, centered on the z -axis, fitting within the bore of a wiggler, and extending beyond the fringe-field regions at the ends of the wiggler.

For simplicity, we will discuss in this section only the use of circular cylinders. In this case, our strategy is illustrated in Figure 3. Specifically, and in summary, we will find that surface methods have the following virtues:

- Only functions with known (orthonormal) completeness properties and known (optimal) convergence properties are employed.
- The Maxwell equations are exactly satisfied.
- The results are manifestly analytic in all variables.
- The error is globally controlled. Fields that satisfy the Laplace equation (are harmonic functions) take their extrema on boundaries. Both the exact and computed fields satisfy the Laplace equation. Therefore their difference, the error field, also satisfies the Laplace equation, and must take its extrema on the boundary. But this is precisely where a controlled fit is made. Thus, the error on the boundary is controlled, and the interior error must be even smaller.
- Because fields take their extrema on boundaries, interior values inferred from surface data are relatively insensitive to errors/noise in the surface data. Put another way, the inverse Laplacian (Laplace Green function), which relates interior data to surface data, is *smoothing*. It is this smoothing that we seek to exploit. We will find that the sensitivity to noise in the data decreases rapidly (as some high inverse power of distance) with increasing distance from the surface, and this property improves the accuracy of the high-order interior derivatives needed to compute high-order transfer maps.

3.1 Cylindrical Harmonic Expansions

To continue our discussion, we will need some background on the use of cylindrical harmonic expansions. They will be used to represent both the scalar and vector potentials. We will employ cylindrical coordinates ρ , ϕ , and z with

$$x = \rho \cos \phi, \tag{3.1}$$

$$y = \rho \sin \phi. \tag{3.2}$$

Note, for future use, that (3.1) and (3.2) can be written in the form

$$x + iy = \rho \exp(i\phi), \tag{3.3}$$

from which it follows that

$$\rho^{2\ell} = (x^2 + y^2)^\ell, \tag{3.4}$$

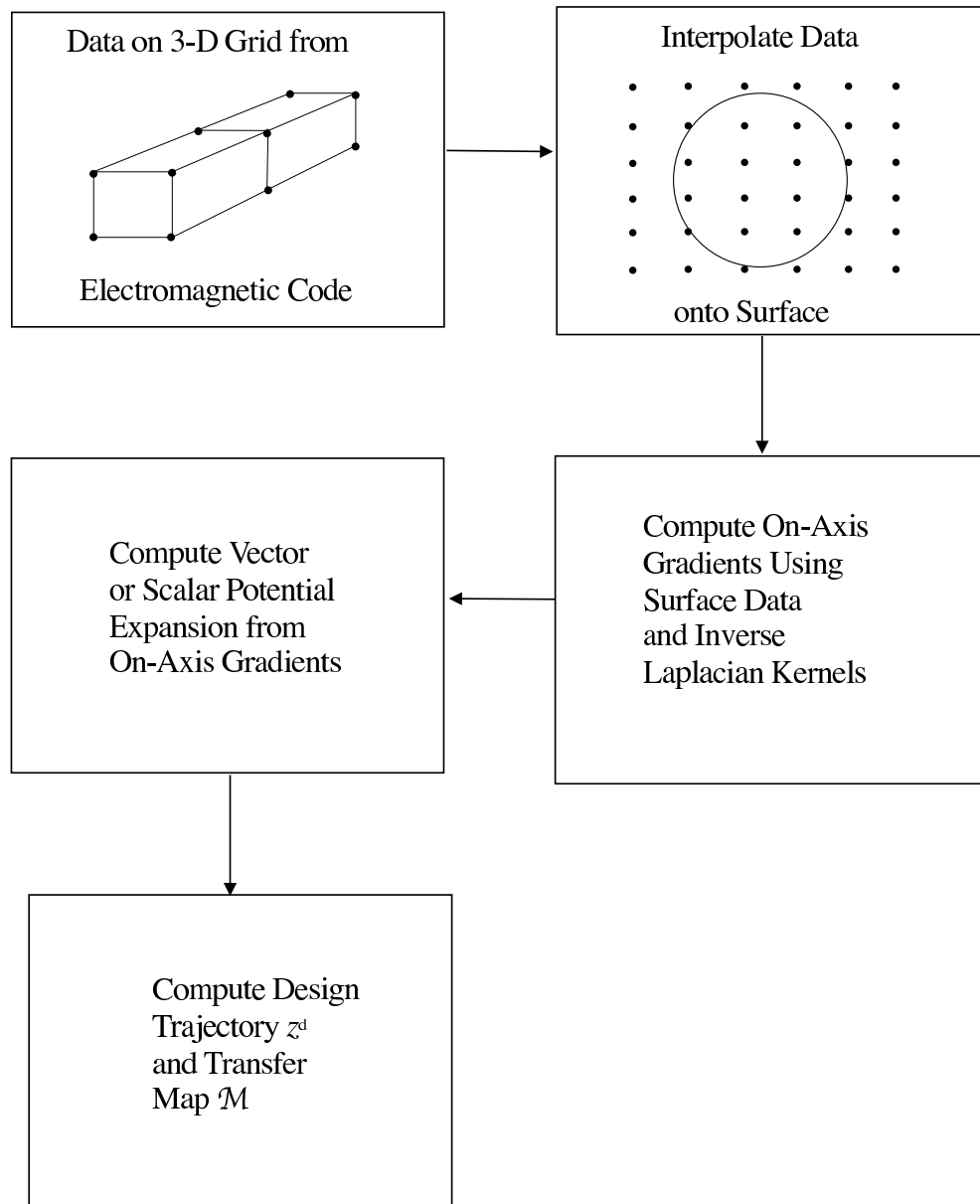


Figure 3: Calculation of realistic design trajectory z^d and its associated realistic transfer map \mathcal{M} based on field data provided on a three-dimensional grid for a real beam-line element. Only a few points on the three-dimensional grid are shown. In this illustration, data from the grid are interpolated onto the surface of a cylinder with circular cross section, and these surface data are then processed to compute the design trajectory and the transfer map. The use of other surfaces is also possible, and may offer various advantages.

$$\rho^m \cos m\phi = \Re[(x + iy)^m], \quad (3.5)$$

$$\rho^m \sin m\phi = \Im[(x + iy)^m]. \quad (3.6)$$

We see that *even* powers of ρ and the combinations $\rho^m \cos m\phi$ and $\rho^m \sin m\phi$ are *analytic* (in fact, polynomial) functions of x and y .

3.1.1 Cylindrical Harmonic Expansion of the Scalar Potential

In view of (2.2) and (2.3) our first goal is to find, in cylindrical coordinates, the general ψ that satisfies Laplace's equation. Begin by recalling that the functions $\exp(im\phi)$ form a complete set for the Hilbert space of functions over the interval $\phi \in [0, 2\pi]$, and the functions $\exp(ikz)$ form a complete set for the Hilbert space of functions over the interval $z \in [-\infty, \infty]$. Therefore any function ψ in the product Hilbert space can be written as a superposition of functions of the form $\Omega_m(k, \rho) \exp(ikz) \exp(im\phi)$ where the functions $\Omega_m(k, \rho)$ are yet to be determined. In cylindrical coordinates the Laplacian has the form

$$\nabla^2 = (1/\rho)(\partial/\partial\rho)(\rho\partial/\partial\rho) + (1/\rho^2)(\partial^2/\partial\phi^2) + \partial^2/\partial z^2. \quad (3.7)$$

Thus if the product $\Omega_m(k, \rho) \exp(ikz) \exp(im\phi)$ is to satisfy Laplace's equation, the functions $\Omega_m(k, \rho)$ must satisfy the modified Bessel equation,

$$(1/\rho)(\partial/\partial\rho)(\rho\partial\Omega_m/\partial\rho) - (m^2/\rho^2)\Omega_m - k^2\Omega_m = 0. \quad (3.8)$$

The solutions to this equation (that are regular for small ρ) are the modified Bessel functions $I_m(k\rho)$. Consequently, in cylindrical coordinates, a general ψ satisfying Laplace's equation and analytic in x, y near the z axis has the expansion

$$\psi(x, y, z) = \sum_{m=-\infty}^{\infty} \int_{-\infty}^{\infty} dk G_m(k) \exp(ikz) \exp(im\phi) I_m(k\rho) \quad (3.9)$$

where the functions $G_m(k)$ are arbitrary.

Our next goal is a Taylor expansion of ψ in the variables x, y with (real) coefficients that depend on z . This can be achieved by using the Taylor expansions for $I_m(w)$,

$$I_m(w) = (1/2)^{|m|} w^{|m|} \sum_{\ell=0}^{\infty} w^{2\ell} / [2^{2\ell} \ell! (\ell + |m|)!]. \quad (3.10)$$

Use of this expansion yields the ultimate result

$$\psi(x, y, z) = \psi_0(x, y, z) + \sum_{m=1}^{\infty} \psi_{m,s}(x, y, z) + \sum_{m=1}^{\infty} \psi_{m,c}(x, y, z). \quad (3.11)$$

The contents of the individual pieces appearing in (3.11), along with conventional names for the elements they describe, are listed below:

Solenoid

$$\psi_0(x, y, z) = \sum_{\ell=0}^{\infty} (-1)^\ell \frac{1}{2^{2\ell} \ell! \ell!} C_0^{[2\ell]}(z) \rho^{2\ell}, \quad (3.12)$$

Normal Multipoles

$$\psi_{m,s}(x, y, z) = \sin(m\phi) \sum_{\ell=0}^{\infty} (-1)^\ell \frac{m!}{2^{2\ell} \ell! (\ell + m)!} C_{m,s}^{[2\ell]}(z) \rho^{2\ell+m}, \quad (3.13)$$

Skew Multipoles

$$\psi_{m,c}(x, y, z) = \cos(m\phi) \sum_{\ell=0}^{\infty} (-1)^\ell \frac{m!}{2^{2\ell} \ell! (\ell + m)!} C_{m,c}^{[2\ell]}(z) \rho^{2\ell+m}. \quad (3.14)$$

Here we have employed the notation

$$C_0^{[n]}(z) = (\partial_z)^n C_0^{[0]}(z), \quad (3.15)$$

$$C_{m,c}^{[n]}(z) = (\partial_z)^n C_{m,c}^{[0]}(z), \quad (3.16)$$

$$C_{m,s}^{[n]}(z) = (\partial_z)^n C_{m,s}^{[0]}(z). \quad (3.17)$$

The functions/coefficients $C_0^{[0]}(z)$, $C_{m,c}^{[0]}(z)$, and $C_{m,s}^{[0]}(z)$, called *on-axis gradients*, are related to the Fourier transforms of the functions $G_m(k)$. They are all real if ψ is real, may be chosen independently, and any such choice produces a harmonic function when employed in (3.11). Again in the language of multipoles, $C_0^{[0]}(z)$ describes a solenoid, the $C_{m,s}^{[0]}(z)$ describe *normal* multipoles, and the $C_{m,c}^{[0]}(z)$ describe *skew* multipoles. Specifically, $m = 1$ for dipoles, $m = 2$ for quadrupoles, $m = 3$ for sextuples, etc.²

Finally, we observe that all the terms in (3.12) through (3.14) are sums of quantities of the form ρ^{2n} , or $\rho^m \cos(m\phi)$ or $\rho^m \sin(m\phi)$ multiplied by powers of ρ^2 , with z -dependent coefficients $C_0^{[2\ell]}(z)$, $C_{m,c}^{[2\ell]}(z)$, and $C_{m,s}^{[2\ell]}(z)$. Thus, in view of (3.4) through (3.6), we have achieved our goal of finding a Taylor expansion for $\psi(x, y, z)$ in powers of x, y with coefficients that depend on z .

²Strictly speaking, dipoles are not *straight* beam-line elements because the design orbit for a dipole is curved. They are best treated using the methods to be described in Section 4. However, the design orbit in a small-amplitude wiggler is essentially straight and the field is essentially described by $m = 1$ terms with the $C_{1,s}^{[0]}(z)$ or $C_{1,c}^{[0]}(z)$ terms being oscillatory in z .

3.1.2 Cylindrical Harmonic Expansion of the Vector Potential

Once cylindrical harmonic expansions, with on-axis gradient coefficients, have been found for the scalar potential ψ , it is possible to construct analogous expansions for the vector potential \mathbf{A} . They too will involve the same on-axis gradient coefficients. In analogy to (3.11), the general \mathbf{A} is given by the sum

$$\mathbf{A} = \mathbf{A}^0 + \sum_{m=1}^{\infty} \mathbf{A}^{m.s} + \sum_{m=1}^{\infty} \mathbf{A}^{m.c}. \quad (3.18)$$

The contents of the individual pieces appearing in (3.18), along again with conventional names for the elements they describe, are listed below. They are in what we call the *symmetric* Coulomb gauge.

Solenoid

$$\begin{aligned} A_x^0 &= -(y/2) \sum_{\ell=0}^{\infty} (-1)^\ell \frac{1}{2^{2\ell} \ell! (\ell+1)!} C_0^{[2\ell+1]}(z) (x^2 + y^2)^\ell \\ &= -(y/2) [C_0^{[1]} - (1/8) C_0^{[3]} (x^2 + y^2) + \dots], \end{aligned} \quad (3.19)$$

$$\begin{aligned} A_y^0 &= (x/2) \sum_{\ell=0}^{\infty} (-1)^\ell \frac{1}{2^{2\ell} \ell! (\ell+1)!} C_0^{[2\ell+1]}(z) (x^2 + y^2)^\ell \\ &= (x/2) [C_0^{[1]} - (1/8) C_0^{[3]} (x^2 + y^2) + \dots], \end{aligned} \quad (3.20)$$

$$A_z^0 = 0. \quad (3.21)$$

Normal Multipoles

$$A_x^{m,s} = (1/2) \Re[(x + iy)^{m+1}] \sum_{\ell=0}^{\infty} (-1)^\ell \frac{m!}{2^{2\ell} \ell! (\ell+m+1)!} C_{m,s}^{[2\ell+1]}(z) (x^2 + y^2)^\ell, \quad (3.22)$$

$$A_y^{m,s} = (1/2) \Im[(x + iy)^{m+1}] \sum_{\ell=0}^{\infty} (-1)^\ell \frac{m!}{2^{2\ell} \ell! (\ell+m+1)!} C_{m,s}^{[2\ell+1]}(z) (x^2 + y^2)^\ell, \quad (3.23)$$

$$A_z^{m,s} = -\Re[(x + iy)^m] \sum_{\ell=0}^{\infty} (-1)^\ell \frac{m!}{2^{2\ell} \ell! (\ell+m)!} C_{m,s}^{[2\ell]}(z) (x^2 + y^2)^\ell. \quad (3.24)$$

Skew Multipoles

$$A_x^{m,c} = -(1/2)\Im[(x + iy)^{m+1}] \sum_{\ell=0}^{\infty} (-1)^\ell \frac{m!}{2^{2\ell}\ell!(\ell + m + 1)!} C_{m,c}^{[2\ell+1]}(z)(x^2 + y^2)^\ell, \quad (3.25)$$

$$A_y^{m,c} = (1/2)\Re[(x + iy)^{m+1}] \sum_{\ell=0}^{\infty} (-1)^\ell \frac{m!}{2^{2\ell}\ell!(\ell + m + 1)!} C_{m,c}^{[2\ell+1]}(z)(x^2 + y^2)^\ell, \quad (3.26)$$

$$A_z^{m,c} = \Im[(x + iy)^m] \sum_{\ell=0}^{\infty} (-1)^\ell \frac{m!}{2^{2\ell}\ell!(\ell + m)!} C_{m,c}^{[2\ell]}(z)(x^2 + y^2)^\ell. \quad (3.27)$$

3.2 Determination of the On-Axis Gradients from Surface Data

3.2.1 Theory/Procedure

All three-dimensional electromagnetic codes calculate all three components of the field on some three-dimensional grid. Also, such data is in principle available from actual field measurements. In this subsection we will describe how surface methods may be used to compute the on-axis gradients, and therefore also the vector potential, from field data. The surface we will employ will be that of a circular cylinder of radius R centered on the z axis.

More specifically, this subsection describes how the $m > 0$ on-axis gradients can be determined based on B_n values specified on the cylindrical surface. In principle the $m = 0$ (solenoid) case can also be treated in this way. But it is probably better to treat the $m = 0$ case using the values of B_z on the cylindrical surface since the field of a solenoid is primarily longitudinal.

Suppose the magnetic field $\mathbf{B}(x, y, z)$ is interpolated onto the surface $\rho = R$ using values at the grid points near the surface. See Figure 3. Next, from the values on the surface, compute $B_\rho(x, y, z) = B_\rho(R, \phi, z)$, the component of $\mathbf{B}(x, y, z)$ *normal* to the surface. We will now see how to compute the on-axis gradients from a knowledge of $B_\rho(R, \phi, z)$.

From this known function form the functions $\tilde{B}_\rho^\alpha(R, m, z)$, with $\alpha = s$ or c , by the rules

$$\tilde{B}_\rho^s(R, m, z) = (1/\pi) \int_0^{2\pi} d\phi \sin(m\phi) B_\rho(R, \phi, z), \quad (3.28)$$

$$\tilde{B}_\rho^c(R, m, z) = (1/\pi) \int_0^{2\pi} d\phi \cos(m\phi) B_\rho(R, \phi, z). \quad (3.29)$$

Next form the functions $\tilde{\tilde{B}}_\rho^\alpha(R, m, k)$ by the rule

$$\tilde{\tilde{B}}_\rho^\alpha(R, m, k) = [1/(2\pi)] \int_{-\infty}^{\infty} dz \exp(-ikz) \tilde{B}_\rho^\alpha(R, m, z). \quad (3.30)$$

Note that the quantities $\tilde{B}_\rho^\alpha(R, m, z)$ are real. Correspondingly, we see from (3.30) that the real part of $\tilde{\tilde{B}}_\rho^\alpha(R, m, k)$ is even in k and the imaginary part is odd in k .

With these definitions in hand, we are ready to state the final results. It can be shown that, for $m > 0$, the on-axis gradients are given by the relations

$$C_{m,\alpha}^{[n]}(z) = i^n (1/2)^m (1/m!) \int_{-\infty}^{\infty} dk [k^{n+m-1}/I'_m(kR)] \tilde{B}_\rho^\alpha(R, m, k) \exp(ikz). \quad (3.31)$$

We have found the on-axis gradients in terms of grid-point values of $\mathbf{B}(x, y, z)$ in the vicinity of the surface $\rho = R$.

3.2.2 Smoothing

In the presence of noise we would expect that the quantities $\tilde{B}_\rho^\alpha(R, m, k)$ would fall off less rapidly with increasing m and with increasing $|k|$ than would otherwise be the case. Also, we observe that the k^{n+m-1} factor in the integrand of (3.31) accentuates this possible high $|k|$ noise. As stated earlier, differentiation amplifies noise.

We will now see that this possible spurious large m and large $|k|$ behavior is *exponentially* damped by the factor $I'(kR)$ appearing in the denominator on the right side of (3.31). Moreover, the greater the value of R , the greater the damping/smoothing. It is therefore desirable to choose as large a value for R as is physically and mathematically possible.

We begin by observing that

$$I_m(-w) = (-1)^m I_m(w). \quad (3.32)$$

Moreover, the large w and large m behaviors of $I_m(w)$ are as follows:

- For fixed m and large $|w|$,

$$|I_m(w)| \simeq (1/\sqrt{2\pi|w|}) \exp(|w|) \text{ as } |w| \rightarrow \infty. \quad (3.33)$$

- For fixed $|w|$ and large m ,

$$\begin{aligned} |I_m(w)| &\simeq (1/\sqrt{2\pi m}) [(e|w|)/(2m)]^m \\ &\simeq (1/2)^m [\sqrt{2\pi m} (m/e)^m]^{-1} |w|^m \\ &\simeq (1/2)^m (1/m!) |w|^m \text{ as } m \rightarrow \infty. \end{aligned} \quad (3.34)$$

Here we have used the Stirling large m approximation

$$m! \simeq \sqrt{2\pi m} (m/e)^m, \quad (3.35)$$

which is already quite accurate for $m \geq 2$.³ Presumably, and as can be checked numerically, the asymptotic behavior of $I'_m(w)$ is similar.

³Note that the final result in (3.34) also follows from retaining only the $\ell = 0$ term in (3.10).

In our case

$$|w| = |k|R, \quad (3.36)$$

and it follows from (3.33), under our assumption about $I'_m(w)$, that

$$|1/I'_m(kR)| \simeq (\sqrt{2\pi|k|R}) \exp(-|k|R) \text{ as } |k| \rightarrow \infty. \quad (3.37)$$

We see that this exponential damping, which is larger the larger the value of R , guarantees the convergence of the integral (3.31) for all n and m , and suppresses whatever high $|k|$ behavior might be present in the $\tilde{B}_\rho^\alpha(R, m, k)$ due to noise in the grid-point data values.

What about the large m behavior? In this case, looking at (3.31), we see that, as well as the result (3.34), we must also take into account the $[(1/2)^m(1/m!)]$ factor appearing in front of the integral. It follows, again under our assumption about $I'_m(w)$, that

$$\begin{aligned} [(1/2)^m(1/m!)]|1/I'_m(kR)| &\simeq [(1/2)^m(1/m!)][(1/2)^m(1/m!)]^{-1}(|k|R)^{-m} \\ &\simeq (|k|R)^{-m} \\ &\simeq \exp[-m \log(|k|R)] \text{ as } m \rightarrow \infty. \end{aligned} \quad (3.38)$$

We see that exponential damping in m is also to be expected.

3.2.3 Numerical Implementation, Benchmarking, and Smoothing Tests

Numerical Implementation

How are the various integrals appearing in Subsection 3.2.1 to be evaluated numerically? Carry out the following steps:

1. Select, as illustrated in Figure 1, a circular cylinder of radius R and length L that fits within the bore of the beam-line element and extends beyond the fringe-field region at the ends of the element. Assume the element is longitudinally centered about $z = 0$. Construct a *cylindrical* grid of $N_\phi \times N_z$ points by selecting points on the cylinder equally spaced in ϕ and also equally spaced in z .
2. We assume there is also a three-dimensional *rectangular* grid, associated with the electromagnetic solver, on which the values of $\mathbf{B}(x, y, z)$ have been found by the solver. We call this grid the *solver* grid. For each cylindrical grid point interpolate $\mathbf{B}(x, y, z)$ values at nearby solver grid points, using for example cubic interpolation, to obtain associated cylindrical grid-point values $\mathbf{B}(R, \phi_j, z_k)$. See Figure 3.
3. From the values $\mathbf{B}(R, \phi_j, z_k)$ construct associated values of $B_\rho(R, \phi_j, z_k)$.
4. Approximate the angular Fourier transforms (3.28) and (3.29) by simple summation. For example, make the approximation

$$\tilde{B}_\rho^s(R, m, z_k) \simeq (1/\pi)(1/N_\phi) \sum_{j=1}^{N_\phi} \sin(m\phi_j) B_\rho(R, \phi_j, z_k). \quad (3.39)$$

According to discrete angular Fourier transform theory, this approximation gives excellent results provided the actual Fourier coefficients fall off sufficiently rapidly for large m , which can be shown to be the case for fields of physical interest.

5. Use cubic splines and the N_z values $\tilde{B}_\rho^\alpha(R, m, z_k)$ to produce *differentiable* functions ${}^d\tilde{B}_\rho^\alpha(R, m, z)$.
6. Approximate the integrals (3.30) to obtain approximate values ${}^d\tilde{B}_\rho^\alpha(R, m, k_\ell)$ by making the definitions

$$\tilde{B}_\rho^\alpha(R, m, k_\ell) \simeq {}^d\tilde{B}_\rho^\alpha(R, m, k_\ell) = [1/(2\pi)] \int_{-L/2}^{L/2} dz \exp(-ik_\ell z) {}^d\tilde{B}_\rho^\alpha(R, m, z). \quad (3.40)$$

Here we have also set up an equally-spaced grid in k space with N_k points and ends $\pm K$. Moreover, the integrals on the right side of (3.40) are to be performed analytically, which is possible for spline fits. Indeed, it is possible to construct *fast* spline-based Fourier transform routines. The use of spline-based Fourier transforms eliminates *aliasing Nyquist* sidebands. Finally, the value of L is to be chosen sufficiently large for the fringe-field values at the element ends to be sufficiently small, thereby assuring good convergence.

7. Use the N_k values ${}^d\tilde{B}_\rho^\alpha(R, m, k_\ell)$ to produce the N_k values $\hat{C}_{m,\alpha}^{[n]}(k_\ell)$ defined by the relations

$$\hat{C}_{m,\alpha}^{[n]}(k_\ell) = [k_\ell^{n+m-1}/I'_m(k_\ell R)] {}^d\tilde{B}_\rho^\alpha(R, m, k_\ell). \quad (3.41)$$

Use cubic splines and the N_k values $\hat{C}_{m,\alpha}^{[n]}(k_\ell)$ to produce the *differentiable* functions ${}^d\hat{C}_{m,\alpha}^{[n]}(k)$.

8. Finally, approximate the integrals (3.31) by writing

$$C_{m,\alpha}^{[n]}(z) \simeq i^n (1/2)^m (1/m!) \int_{-K}^K dk {}^d\hat{C}_{m,\alpha}^{[n]}(k) \exp(ikz). \quad (3.42)$$

The integrals on the right of (3.42) are to be evaluated using spline-based Fourier transform routines. The value of K is to be chosen sufficiently large for the factor $[1/I'_m(kR)]$ to provide adequate convergence.

Benchmarking

There are least five ways to test/benchmark the procedures just described:

- (a) There are *magnetic charge* configurations for which both $\mathbf{B}(x, y, z)$ and the $C_{m,\alpha}^{[n]}(z)$ can be computed analytically. One of the simplest is that of a magnetic monopole doublet.

A cylindrical grid can then be set up and the values $B_\rho(R, \phi_j, z_k)$ can be evaluated analytically. Alternatively, a rectangular (solver) grid can also be set up and simulated values of $\mathbf{B}(x, y, z)$ at the rectangular grid points can be set up analytically. Following steps 2 and 3, these values can then be used to set up the values $B_\rho(R, \phi_j, z_k)$. Either way, following steps 4 through 8, compute the $C_{m,\alpha}^{[n]}(z)$ numerically, and compare these numerical results with those obtained analytically.

- (b) Use the $C_{m,\alpha}^{[n]}(z)$ computed numerically as in (a) to form the scalar potential $\psi(x, y, z)$ specified by (3.11). From this ψ , compute $\mathbf{B}(x, y, z)$ using (2.2) at *interior* (to the cylinder) points. Alternatively, compute \mathbf{B} at interior points using

$$\mathbf{B} = \nabla \times \mathbf{A} \tag{3.43}$$

with $\mathbf{A}(x, y, z)$ given by (3.18). Compare the fields $\mathbf{B}(x, y, z)$ thus found numerically with the interior fields computed analytically as in (a).

- (c) Use the $C_{m,\alpha}^{[n]}(z)$ computed both analytically and numerically as in (a) to compute associated maps \mathcal{M} by integrating, in each instance, the equations in Subsections 1.7.1 and 1.7.2. Two maps, \mathcal{M} and \mathcal{M}' , can be conveniently compared by forming the product $\mathcal{M}^{-1}\mathcal{M}'$ and examining how close this resulting map is to the identity map \mathcal{I} .
- (d) There are *current* distributions for which both $\mathbf{B}(x, y, z)$ and the Taylor coefficients for $\mathbf{A}(x, y, z)$ can be computed numerically. Lambertson type quadrupoles provide an example. Follow steps 1 through 8 as in (a) to compute $\mathbf{A}(x, y, z)$ using (3.18), and compare the resulting $\mathbf{A}(x, y, z)$ with that found numerically from the current distribution. To make this comparison the two vector potentials must be brought to the same gauge, say the Poincaré-Coulomb gauge, if they are not already in a common gauge. See Subsection 3.3.
- (e) Use a field solver to find the fields on some solver grid for some beam-line element of interest. Execute steps 1 through 8. Use the $C_{m,\alpha}^{[n]}(z)$ computed numerically to form the scalar potential $\psi(x, y, z)$ specified by (3.11). From this ψ , compute $\mathbf{B}(x, y, z)$ using (2.2) at interior solver grid points. Alternatively, use (3.43) to compute \mathbf{B} . Compare these so-obtained \mathbf{B} values with those provided by the solver itself at the same interior points. This comparison also tests how “Maxwellian” the $\mathbf{B}(x, y, z)$ solver values actually are. (Note that the surface method uses only solver field values in the vicinity of the cylinder $\rho = R$.)

It has been found in practice that when performed, providing N_ϕ , N_z , N_k , L , and K are sufficiently large, any of the above tests is passed to many significant figures. At this point one last remark is called for. In our calculations we have used for S only the *curved* part of the cylinder, and have ignored any possible $\mathbf{e}_z \cdot \mathbf{B}$ contributions from end caps. In principle, they should also be included, and they can be if desired. However, if L is sufficiently large, \mathbf{B} is so small at the ends of the cylinder that possible end-cap contributions are negligible.

Smoothing Tests

There are at least two ways to test how sensitive surface methods are to noise in the field values at solver grid points:

- Use a field solver to find the fields on some solver grid for some beam-line element of interest. Execute steps 1 through 8 to find the associated $C_{m,\alpha}^{[n]}(z)$. To model the effect of noise, modify the fields at the solver grid points in some small and random way. For example, at each solver grid point one might make the replacement

$$\mathbf{B}(x, y, z) \rightarrow \mathbf{B}(x, y, z) + |\mathbf{B}(x, y, z)|\epsilon(x, y, z)\mathbf{n}(x, y, z). \quad (3.44)$$

Here the $\mathbf{n}(x, y, z)$ are unit vectors to be chosen randomly at each solver grid point, and at each solver grid point $\epsilon(x, y, z)$ is to be chosen randomly from a small interval, say $\epsilon(x, y, z) \in [-.01, .01]$. Use the modified fields to find associated modified $C_{m,\alpha}^{[n]}(z)$. Repeat this operation for several random number seeds. Examine how the so generated ensemble of modified $C_{m,\alpha}^{[n]}(z)$ functions compares to the $C_{m,\alpha}^{[n]}(z)$ functions computed in the absence of noise. If desired, compute also the associated maps \mathcal{M} , and examine how they compare.

- Examine how sensitive the $C_{m,\alpha}^{[n]}(z)$ functions, and the associated interior \mathbf{B} values given by (2.2) with ψ given by (3.11), are to the value of $\mathbf{B}(x, y, z)$ at any given solver grid point. Do this by setting all solver grid point field values to zero save for one, which is taken to be a randomly chosen unit vector. Let z^* be the value of z for the solver grid point at which the field is taken to be nonzero. It is expected that the contribution of any solver grid point field value should fall off with distance from the location of the solver grid point. For this reason, arrange to have $z^* \approx 0$.

When the first test has been performed for feasible values of the radius R , it has been found that a 1% error in the grid point field values produces an associated $\approx 1\%$ error in the $C_{m,\alpha}^{[n]}(z)$ and in \mathcal{M} . Consequently, in the cases tested, it has been verified that smoothing does indeed compensate for the differentiation-associated amplification of numerical noise.

With regard to the second test, analytic calculations suggest that the effect of a local disturbance in the scalar potential (on the cylindrical surface $\rho = R$) of the form

$$\Delta\psi(R, \phi, z) = \delta(\phi)\delta(z) \quad (3.45)$$

should fall off like $\exp[-\pi|z|/(2R)]$ as $|z| \rightarrow \infty$. Similar results should hold for the fall off with distance of the contribution made by any solver grid point field value.

3.3 Use of Minimum Vector Potential for End-Field Terminations

3.3.1 Need for Termination Approximation

The symplectic transfer map \mathcal{M} relating w^{in} and w^{fin} at the entry of the leading fringe-field region and exit of the trailing fringe-field region is *independent* of the choice of gauge for the vector potential \mathbf{A} provided \mathbf{A} *vanishes* at the entry of the leading fringe-field region and at the exit of the trailing fringe-field region.⁴ If the vector potential does not vanish at these effective element ends, the map \mathcal{M} is gauge dependent and therefore not uniquely defined. In practice, \mathbf{A} does not vanish exactly, or perhaps not even approximately, at these points either due to the way in which it was calculated or because \mathbf{B} itself does not exactly vanish at these points. (In general for real beam-line elements \mathbf{B} vanishes only at infinity.) For practical calculations, in the approximation of individually isolated beam-line elements, it is necessary to terminate \mathbf{A} , in some well-defined way, at these points.

3.3.2 Symplecticity and the Termination Approximation Imply Discontinuities in the Mechanical Momenta

Moreover, the *canonical* and *mechanical* momenta are related by the rules

$$P_x^{\text{can}} - A_x^s = P_x^{\text{mech}}, \quad (3.46)$$

$$P_y^{\text{can}} - A_y^s = P_y^{\text{mech}}. \quad (3.47)$$

Let us consider, for example, what the *matching* conditions should be *before entry* and *after entry* into a leading fringe-field region. Introduce, for example for the X coordinate before and after entry, the symbols X^{ben} and X^{aen} . Then it is natural to require for the spatial coordinates the conditions

$$X^{\text{aen}} = X^{\text{ben}}, \text{ and similarly for the } Y \text{ and } \tau \text{ coordinates.} \quad (3.48)$$

What about the momentum coordinates? In analogy to (3.48), we demand the conditions

$$P_x^{\text{canaen}} = P_x^{\text{canben}}, \text{ and similarly for the } P_y^{\text{can}} \text{ and } P_\tau \text{ momenta.} \quad (3.49)$$

Note that, taken together, the relations (3.48) and (3.49) comprise a symplectic map relating before and after conditions, namely the identity map.

But, before entry, we wish to make the assumption/approximation that A_x^{sben} and A_y^{sben} vanish. It follows from (3.46) and (3.47) that there must be the relations

$$P_x^{\text{canben}} = P_x^{\text{mechben}}, \quad (3.50)$$

⁴Here we use the symbol $w = (X, Y, \tau, P_x, P_y, P_\tau)$ to denote phase-space variables because now we wish to use the symbol z to denote the longitudinal Cartesian variable, which, as discussed earlier, we employ as the independent variable

$$P_y^{\text{canben}} = P_y^{\text{mechben}}. \quad (3.51)$$

Also, (3.46) and (3.47) have the after entry counterparts

$$P_x^{\text{canaen}} - A_x^{\text{saen}} = P_x^{\text{mechaen}}, \quad (3.52)$$

$$P_y^{\text{canaen}} - A_y^{\text{saen}} = P_y^{\text{mechaen}}. \quad (3.53)$$

From (3.50) through (3.53) we see that the matching relations (3.49) require the relations

$$P_x^{\text{mechaen}} = P_x^{\text{canaen}} - A_x^{\text{saen}} = P_x^{\text{canben}} - A_x^{\text{saen}} = P_x^{\text{mechben}} - A_x^{\text{saen}}, \quad (3.54)$$

$$P_y^{\text{mechaen}} = P_y^{\text{canaen}} - A_y^{\text{saen}} = P_y^{\text{canben}} - A_y^{\text{saen}} = P_y^{\text{mechben}} - A_y^{\text{saen}}. \quad (3.55)$$

Continuity in the canonical variables, as required for symplecticity, and the approximations made in terminating the vector potential, imply an unavoidable entry discontinuity in the mechanical momenta P_x^{mech} and P_y^{mech} . A similar discontinuity occurs upon exiting a trailing fringe-field region.

3.3.3 Use of Minimum Vector Potential to Minimize Discontinuities

While, as we have seen, the approximations implied by termination introduce discontinuities in the mechanical momenta, these discontinuities can be minimized by choosing a gauge for which \mathbf{A}^{saen} is as *small* as possible consistent with the requirement that

$$\nabla \times \mathbf{A}^{\text{saen}} = \mathbf{B}^{\text{saen}}. \quad (3.56)$$

The gauge that meets this criterion is the Poincaré-Coulomb gauge. Let $\mathbf{A}^{\text{saenPC}}$ be the vector potential in this gauge. In the vicinity of the entry point on the design orbit it satisfies the conditions

$$\nabla \times \mathbf{A}^{\text{saenPC}} = \mathbf{B}^{\text{saen}}, \quad (3.57)$$

$$\nabla \cdot \mathbf{A}^{\text{saenPC}} = 0, \quad (3.58)$$

$$\mathbf{r}' \cdot \mathbf{A}^{\text{saenPC}} = 0, \quad (3.59)$$

and is *unique*. Here \mathbf{r}' is a *local* position vector whose origin is the entry point on the design orbit.

We also refer to $\mathbf{A}^{\text{saenPC}}$ as the *minimum* vector potential that satisfies (3.56). It is minimal in the following senses:

- It vanishes at the entry point on the design orbit. Therefore, on the design orbit, there is no discontinuity in the mechanical momentum.

- It is proportional to the magnetic field \mathbf{B}^{saen} in the vicinity of the entry point on the design orbit, and therefore is small if $|\mathbf{B}^{\text{saen}}|$ is small, as we would hope is the case. More specifically, suppose that $\mathbf{A}^{\text{saenPC}}$ is expanded in the form

$$\mathbf{A}^{\text{saenPC}} = \sum_{d=0}^{\infty} \mathbf{A}_d^{\text{saenPC}}, \quad (3.60)$$

and that similarly \mathbf{B}^{saen} is expanded in the form

$$\mathbf{B}^{\text{saen}} = \sum_{d=0}^{\infty} \mathbf{B}_d^{\text{saen}}. \quad (3.61)$$

Here the vectors $\mathbf{A}_d^{\text{saenPC}}$ and $\mathbf{B}_d^{\text{saen}}$ are *homogeneous* of degree d in the components of \mathbf{r}' . Then there are the relations

$$\mathbf{A}_0^{\text{saenPC}} = 0, \quad (3.62)$$

$$\mathbf{A}_d^{\text{saenPC}} = -[1/(d+1)][\mathbf{r}' \times \mathbf{B}_{d-1}^{\text{saen}}] \text{ for } d = 1, 2, \dots. \quad (3.63)$$

- Suppose that any vector potential \mathbf{A}^{saen} that satisfies (3.56) is written in the form

$$\mathbf{A}^{\text{saen}} = \sum_{d=0}^{\infty} \mathbf{A}_d^{\text{saen}}. \quad (3.64)$$

Then setting $\mathbf{A}_d^{\text{saen}} = \mathbf{A}_d^{\text{saenPC}}$ *minimizes* the integrals

$$\|\mathbf{A}_d^{\text{saen}}\|^2 = \int d\Omega \mathbf{A}_d^{\text{saen}} \cdot \mathbf{A}_d^{\text{saen}} \quad (3.65)$$

where $\int d\Omega$ denotes integration over solid angle.

3.3.4 Gauge Transformations

Need for Changing Gauges

Although use of the Poincaré-Coulomb gauge is optimal at entry to and exit from fringe-field regions, its use is not convenient in the region after entry and before exit because $\mathbf{A}^{\text{saenPC}}$ is not *simply* expressible in terms of on-axis gradients.⁵ This seeming problem can be solved by changing, after entry, from the Poincaré-Coulomb gauge to the symmetric

⁵The the relations that specify $\mathbf{A}^{\text{saenPC}}$ in terms of the on-axis gradients generally involve Taylor expansions of the on-axis gradients. The only exception is the symmetric Coulomb gauge vector potential for a solenoid. As can be verified from (3.19) through (3.21), it is also in the Poincaré-Coulomb gauge. The symmetric Coulomb gauge and the Poincaré-Coulomb gauge are the same for a solenoid.

Coulomb gauge and, before exit, changing back from the symmetric Coulomb gauge to the Poincaré-Coulomb gauge. Thus the transfer map describing the effect of the region after entry and before exit, which we will call \mathcal{M}^{SC} , is to be computed using the the vector potential in the symmetric Coulomb gauge. Moreover, we will see that the two gauge transformations just specified at *entry* and at *exit* can be described by two symplectic maps which we will call \mathcal{M}^{en} and \mathcal{M}^{ex} . The full map \mathcal{M} describing the relation between the initial conditions just before entry and the final conditions just after exit can then be written in the form

$$\mathcal{M} = \mathcal{M}^{en} \mathcal{M}^{SC} \mathcal{M}^{ex}. \quad (3.66)$$

Note that we could have also used some other convenient gauge for the vector potential in the region after entry and before exit. In this case, \mathcal{M}^{en} and \mathcal{M}^{ex} would also have been different. But the full map, when computed by the relation analogous to (3.66), would be *unchanged*. Thus, when the *uniquely* defined Poincaré-Coulomb gauge vector potentials are used at entry and exit, the full map \mathcal{M} is, in fact, gauge independent.

Gauge Transformations are Symplectic Maps

What remains to be described is how to compute the maps \mathcal{M}^{en} and \mathcal{M}^{ex} . We will discuss the general problem of changing gauges at various points during the course of integrating a trajectory and computing an associated transfer map about that trajectory.

Suppose the gauge is to be *changed* at the point $z = z^c$. (Recall that we are using z as the *independent* variable.) Let X^b, Y^b , and τ^b denote the coordinate functions *before* the change, and let X^a, Y^a , and τ^a denote the coordinate functions *after* the change. Also, let $\mathbf{A}^{sb}(X^b, Y^b; z)$ and $\mathbf{A}^{sa}(X^a, Y^a; z)$ be the vector potentials before ($z < z^c$) and after ($z > z^c$) the change point z^c . Finally, let $P_x^{canb}, P_y^{canb}, P_\tau^{canb}$ be the canonical momentum functions before the change, and let $P_x^{cana}, P_y^{cana}, P_\tau^{cana}$ be the canonical momentum functions after the change. In terms of these quantities, the before and after Hamiltonians H^b and H^a are given as follows:

Before, for $z < z^c$,

$$\begin{aligned} H^b = & -(1/\ell) \times \\ & \{[1 - (2P_\tau^{canb}/\beta_0) + (P_\tau^{canb})^2 - (P_x^{canb} - A_x^{sb})^2 - (P_y^{canb} - A_y^{sb})^2]^{1/2} \\ & + A_z^{sb} + (P_\tau^{canb}/\beta_0) - 1\}. \end{aligned} \quad (3.67)$$

After, for $z > z^c$,

$$\begin{aligned}
H^a = & -(1/\ell) \times \\
& \{[1 - (2P_\tau^{cana}/\beta_0) + (P_\tau^{cana})^2 - (P_x^{cana} - A_x^{sa})^2 - (P_y^{cana} - A_y^{sa})^2]^{1/2} \\
& + A_z^{sa} + (P_\tau^{cana}/\beta_0) - 1\}.
\end{aligned} \tag{3.68}$$

What should be the matching relations between the phase-space quantities before and after? Since the choice of gauge should have no physical effect, there is the immediate requirement that the coordinate functions be continuous:

$$\begin{aligned}
X^a(z) &= X^b(z) \text{ when } z = z^c, \\
Y^a(z) &= Y^b(z) \text{ when } z = z^c, \\
\tau^a(z) &= \tau^b(z) \text{ when } z = z^c.
\end{aligned} \tag{3.69}$$

For the same reason, we require that the velocities, and hence the mechanical momenta, be continuous. From (3.46), for example, we see that this requirement is equivalent to the matching relation

$$P_x^{cana} - A_x^{sa} = P_x^{canb} - A_x^{sb} \text{ when } z = z^c, \tag{3.70}$$

which can be rewritten in the form

$$P_x^{cana} = P_x^{canb} + (A_x^{sa} - A_x^{sb}) \text{ when } z = z^c. \tag{3.71}$$

Similarly, there is the matching relation

$$P_y^{cana} = P_y^{canb} + (A_y^{sa} - A_y^{sb}) \text{ when } z = z^c. \tag{3.72}$$

Finally, the total energy cannot change under a gauge transformation, and therefore there is the matching relation

$$P_\tau^{cana} = P_\tau^{canb} \text{ when } z = z^c. \tag{3.73}$$

We assume there is some common overlap region where both \mathbf{A}^{sb} and \mathbf{A}^{sa} are defined. Since they both give rise to the same magnetic field, there is the relation

$$\nabla \times (\mathbf{A}^{sa} - \mathbf{A}^{sb}) = 0. \tag{3.74}$$

It follows that there is a *gauge* function χ such that

$$\mathbf{A}^{sa} - \mathbf{A}^{sb} = \nabla\chi. \tag{3.75}$$

Note that, if spatial Taylor expansions about some spatial point on the design orbit are known for both \mathbf{A}^{sb} and \mathbf{A}^{sa} , as is the case for our applications, then it is straight forward to find an associated Taylor expansion for χ .

With the use of (3.75) the relations (3.71) and (3.72) can be rewritten in the form

$$\begin{aligned} P_y^{cana} &= P_y^{canb} + (\partial\chi/\partial X) \text{ when } z = z^c, \\ P_y^{cana} &= P_y^{canb} + (\partial\chi/\partial Y) \text{ when } z = z^c. \end{aligned} \quad (3.76)$$

There is one last step. Let \mathcal{T}^c be the symplectic transformation map defined by the relation

$$\mathcal{T}^c = \exp(: \chi :). \quad (3.77)$$

With the aid of this map it is easily verified that the relations (3.69) and (3.71) through (3.73) can be rewritten in the form

$$\begin{aligned} X^a &= \exp(: \chi :)X^b = \mathcal{T}^c X^b \text{ with } z = z^c, \\ Y^a &= \exp(: \chi :)Y^b = \mathcal{T}^c Y^b \text{ with } z = z^c, \\ \tau^a &= \exp(: \chi :) \tau^b = \mathcal{T}^c \tau^b \text{ with } z = z^c; \end{aligned} \quad (3.78)$$

$$\begin{aligned} P_x^{cana} &= \exp(: \chi :)P_x^{canb} = \mathcal{T}^c P_x^{canb} \text{ with } z = z^c, \\ P_y^{cana} &= \exp(: \chi :)P_y^{canb} = \mathcal{T}^c P_y^{canb} \text{ with } z = z^c, \\ P_\tau^{cana} &= \exp(: \chi :)P_\tau^{canb} = \mathcal{T}^c P_\tau^{canb} \text{ with } z = z^c. \end{aligned} \quad (3.79)$$

We have determined that a change in gauge amounts to making a symplectic transformation.

4 Surface Methods for Curved Beam-Line Elements

Surface methods based on the use of cylinders are appropriate for straight beam-line elements. However, cylinders cannot be employed for elements with large sagitta, such as dipoles, where no straight cylinder would fit within the aperture. For such cases more complicated surfaces are required. For example, Figure 4 shows a bent box with straight end legs. Its surface could be used to treat a dipole with large sagitta. In this case, the bent part of the box would lie within the body of the dipole, and the straight end legs would enclose the fringe-field regions.

But now there is a complication: The cylinder methods succeeded because Laplace's equation is separable in circular and elliptical cylinder coordinates. Consequently, we were able to find a kernel that related the interior vector potential to the normal component of the surface magnetic field. However, there is no bent coordinate system with straight ends for which Laplace's equation is separable.

This problem can in principle be overcome if *both* the normal and tangential components of the magnetic field are known on the surface.⁶ Alternatively and equivalently, it can in

⁶This approach, including the use of Helmholtz decomposition and Dirac magnetic monopoles, was pioneered by *Peter Walstrom*.

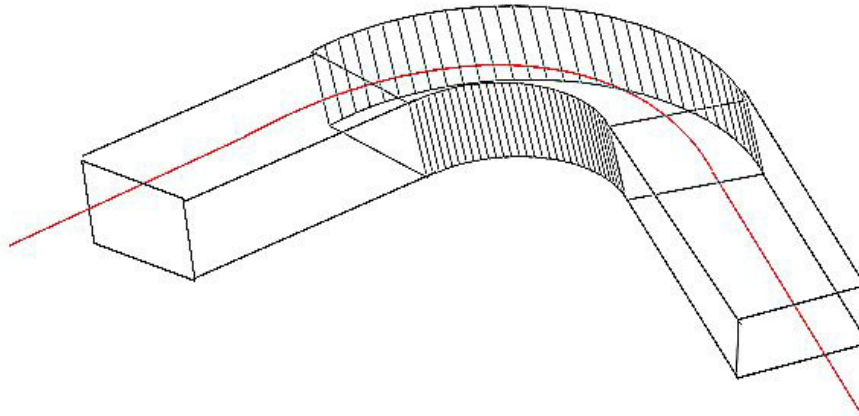


Figure 4: A bent box with straight end legs.

principle be overcome if both the normal component of the magnetic field and the scalar potential for the magnetic field are known on the surface. Such data are in fact provided on a grid by some three-dimensional field solvers, and these data can be interpolated onto the surface. The purpose of this section is to describe how this can be accomplished.

4.1 Mathematical Tools

4.1.1 Helmholtz Decomposition

Suppose V is some simply connected volume in three-dimensional space bounded by a surface S , and suppose $\mathbf{F}(\mathbf{r})$ is some three-dimensional vector field defined in V . Then, according to a theorem of *Helmholtz*, there are scalar and vector potentials $\phi(\mathbf{r})$ and $\mathbf{A}(\mathbf{r})$ such that

$$\mathbf{F}(\mathbf{r}) = -\nabla\phi(\mathbf{r}) + \nabla \times \mathbf{A}(\mathbf{r}) \text{ for } \mathbf{r} \in V. \quad (4.1)$$

Specifically, let $G(\mathbf{r}, \mathbf{r}')$ be the function

$$G(\mathbf{r}, \mathbf{r}') = 1/|\mathbf{r} - \mathbf{r}'|. \quad (4.2)$$

Then, the scalar and vector potentials are given in terms of $\mathbf{F}(\mathbf{r})$, with $\mathbf{r} \in V$, by the relations

$$\phi(\mathbf{r}) = -[1/(4\pi)] \int_S dS' \mathbf{n}' \cdot \mathbf{F}(\mathbf{r}')G(\mathbf{r}, \mathbf{r}') + [1/(4\pi)] \int_V d^3\mathbf{r}' G(\mathbf{r}, \mathbf{r}')\nabla' \cdot \mathbf{F}(\mathbf{r}'), \quad (4.3)$$

$$\mathbf{A}(\mathbf{r}) = -[1/(4\pi)] \int_S dS' [\mathbf{n}' \times G(\mathbf{r}, \mathbf{r}') \mathbf{F}(\mathbf{r}')] + [1/(4\pi)] \int_V d^3\mathbf{r}' G(\mathbf{r}, \mathbf{r}') \nabla' \times \mathbf{F}(\mathbf{r}'). \quad (4.4)$$

Here \mathbf{n}' is the outward normal to S at the point \mathbf{r}' . We emphasize, as is evident from (4.1), (4.3), and (4.4), that for $\mathbf{r} \in V$ the vector field \mathbf{F} is completely specified in terms of the divergence and curl of \mathbf{F} within V and the values of \mathbf{F} on the bounding surface S . No information is required outside of V .

We will apply this result to the case for which \mathbf{F} is the magnetic field \mathbf{B} . Suppose that $\mathbf{B}(\mathbf{r})$ is source free when \mathbf{r} is within V , as will be true for the magnetic field in an evacuated beam pipe. In that case there will be the relations

$$\nabla \cdot \mathbf{F}(\mathbf{r}) = 0 \text{ for } \mathbf{r} \in V \quad (4.5)$$

and

$$\nabla \times \mathbf{F}(\mathbf{r}) = 0 \text{ for } \mathbf{r} \in V \quad (4.6)$$

so that only the surface terms appear in (4.3) and (4.4). With \mathbf{F} replaced by \mathbf{B} , they then become

$$\phi^n(\mathbf{r}) = -[1/(4\pi)] \int_S dS' \mathbf{n}' \cdot \mathbf{B}(\mathbf{r}') G(\mathbf{r}, \mathbf{r}'), \quad (4.7)$$

$$\mathbf{A}^t(\mathbf{r}) = -[1/(4\pi)] \int_S dS' [\mathbf{n}' \times \mathbf{B}(\mathbf{r}')] G(\mathbf{r}, \mathbf{r}'). \quad (4.8)$$

Correspondingly, (4.1) takes the form

$$\mathbf{B}(\mathbf{r}) = -\nabla \phi^n(\mathbf{r}) + \nabla \times \mathbf{A}^t(\mathbf{r}) \text{ for } \mathbf{r} \in V. \quad (4.9)$$

Here we have added the superscripts n and t to emphasize that $\phi^n(\mathbf{r})$ and $\mathbf{A}^t(\mathbf{r})$ depend, respectively, only on the *normal* and *tangential* components of \mathbf{B} on S .

We also take the opportunity at this point to note that $G(\mathbf{r}, \mathbf{r}')$ as given by (4.2), and for fixed \mathbf{r}' , is an *analytic* function of the components of \mathbf{r} for $\mathbf{r} \neq \mathbf{r}'$. It follows from the representations (4.7) and (4.8), under very mild assumptions on the surface behavior of $\mathbf{B}(\mathbf{r})$, boundedness and continuity will do, that $\phi^n(\mathbf{r})$ and $\mathbf{A}^t(\mathbf{r})$ are *analytic* functions of the components of \mathbf{r} for \mathbf{r} within V . Correspondingly, from (4.9), $\mathbf{B}(\mathbf{r})$ must then also be analytic for \mathbf{r} within V .

4.1.2 Use of Dirac Magnetic Monopoles

For a Hamiltonian treatment of trajectories, we need a vector potential $\mathbf{A}(\mathbf{r})$ such that

$$\mathbf{B}(\mathbf{r}) = \nabla \times \mathbf{A}(\mathbf{r}). \quad (4.10)$$

As it stands, (4.9) is not of this form due to the term $-\nabla\phi^n(\mathbf{r})$. What we need is an associated vector potential term $\mathbf{A}^n(\mathbf{r})$ with the property

$$\nabla \times \mathbf{A}^n(\mathbf{r}) = -\nabla\phi^n(\mathbf{r}). \quad (4.11)$$

Then (4.10) will be achieved with

$$\mathbf{A} = \mathbf{A}^n + \mathbf{A}^t. \quad (4.12)$$

We will see that the desired vector potential term \mathbf{A}^n can be found with the use of *Dirac* magnetic monopole vector potentials.

Inspection of $\phi^n(\mathbf{r})$, as given by (4.7), shows that it appears to arise from a distribution of magnetic monopoles described by a magnetic charge surface density spread over the surface S with the surface charge density given by

$$B_n(\mathbf{r}') = \mathbf{n}' \cdot \mathbf{B}(\mathbf{r}'). \quad (4.13)$$

Therefore, it should be possible to find an equivalent vector potential based on the vector potential for a magnetic monopole.

This is indeed the case. It can be shown that a suitable \mathbf{A}^n is given by the relation

$$\mathbf{A}^n(\mathbf{r}) = \int_S dS' B_n(\mathbf{r}') \mathbf{G}^n(\mathbf{r}; \mathbf{r}', \mathbf{m}') \quad (4.14)$$

where the kernel \mathbf{G}^n is defined by the rule

$$\mathbf{G}^n(\mathbf{r}; \mathbf{r}', \mathbf{m}') = \{\mathbf{m}'(\mathbf{r}') \times (\mathbf{r} - \mathbf{r}')\} / \{4\pi|\mathbf{r} - \mathbf{r}'| [|\mathbf{r} - \mathbf{r}'| - \mathbf{m}'(\mathbf{r}') \cdot (\mathbf{r} - \mathbf{r}')]\}. \quad (4.15)$$

The construction of \mathbf{G}^n is based on the use of magnetic monopoles situated at the points $\mathbf{r}' \in S$ with Dirac strings that extend to infinity along straight lines in the directions \mathbf{m}' . In evaluating the integral (4.14) it necessary to specify $\mathbf{m}'(\mathbf{r}')$ as \mathbf{r}' varies over S . There is considerable freedom in doing so, and different choices simply result in different gauges for $\mathbf{A}^n(\mathbf{r})$. There is only one major consideration: As described below, no string should intersect the volume V . For many geometries a convenient choice is to require that $\mathbf{m}'(\mathbf{r}')$ be normal to and point outward from S ,

$$\mathbf{m}'(\mathbf{r}') = \mathbf{n}'(\mathbf{r}'). \quad (4.16)$$

Other choices may also be convenient and useful.

At this point we can take pleasure in observing that $\mathbf{G}^n(\mathbf{r}; \mathbf{r}', \mathbf{m}')$, and consequently $\mathbf{A}^n(\mathbf{r})$, have several desirable properties: First, as long as the Dirac strings for $\mathbf{r}' \in S$ do not intersect V , the functions $\mathbf{G}^n(\mathbf{r}; \mathbf{r}', \mathbf{m}')$, for every $\mathbf{r}' \in S$, are analytic in \mathbf{r} for all $\mathbf{r} \in V$. It follows from (4.14), under mild conditions on $B_n(\mathbf{r}')$ for $\mathbf{r}' \in S$, that $\mathbf{A}^n(\mathbf{r})$ is

analytic in V . Second, since the kernel $\mathbf{G}^n(\mathbf{r}; \mathbf{r}', \mathbf{m}')$ is essentially the vector potential for a Dirac magnetic monopole, it can be shown to have, for $\mathbf{r} \in V$, the properties

$$\nabla \cdot [\mathbf{G}^n(\mathbf{r}; \mathbf{r}', \mathbf{m}')] = 0, \quad (4.17)$$

$$\nabla \times [\nabla \times \mathbf{G}^n(\mathbf{r}; \mathbf{r}', \mathbf{m}')] = 0. \quad (4.18)$$

It follows from (4.14), again under mild conditions on $B_n(\mathbf{r}')$, that $\mathbf{A}^n(\mathbf{r})$ has these same properties,

$$\nabla \cdot [\mathbf{A}^n(\mathbf{r})] = 0, \quad (4.19)$$

$$\nabla \times [\nabla \times \mathbf{A}^n(\mathbf{r})] = 0. \quad (4.20)$$

In practical applications, the surface values $B_n(\mathbf{r}')$ will only be known approximately, and the integrals (4.14) may be evaluated numerically with limited precision. It is comforting to know that, nevertheless, the resulting $\mathbf{A}^n(\mathbf{r})$ will be analytic in V and will satisfy the relations (4.19) and (4.20) exactly no matter what errors are present in the surface values $B_n(\mathbf{r}')$ and no matter how poorly the integrals (4.14) are evaluated. All that matters is that the kernel \mathbf{G}^n be evaluated to high precision.

4.1.3 Use of the Scalar Potential ψ

What can be said about the properties of $\mathbf{A}^t(\mathbf{r})$ as given by (4.8)? It can be shown to be analytic in V and to satisfy properties analogous to (4.19) and (4.20) *provided* (4.8) is evaluated *exactly*. As is the case for (4.14), we would like to have an integral representation for \mathbf{A}^t that has these desired properties no matter how badly the integrals are evaluated. This can be accomplished with the aid of a scalar potential.

Since, by assumption, $\mathbf{B}(\mathbf{r}')$ is curl free for $\mathbf{r}' \in V$, there exists a scalar potential $\psi(\mathbf{r}')$ such that

$$\mathbf{B}(\mathbf{r}') = +\nabla' \psi(\mathbf{r}'). \quad (4.21)$$

[Note, by convention, we have used a minus sign in (4.9) and a plus sign in (4.21). See also (2.2).] Next we observe that (4.8) involves the *tangential* component of $\mathbf{B}(\mathbf{r}')$ on S . Under the assumption that $\mathbf{B}(\mathbf{r}')$ is curl free, knowledge of the tangential component of $\mathbf{B}(\mathbf{r}')$ on S is equivalent to a knowledge of ψ on S . It should therefore be possible to transform (4.8) to an expression involving ψ on S .

This is indeed possible. It can be shown, with the aid of (4.21), that (4.9) can be transformed to become

$$\mathbf{A}^t(\mathbf{r}) = \int_S dS' \psi(\mathbf{r}') \mathbf{G}^t(\mathbf{r}, \mathbf{r}') \quad (4.22)$$

where

$$\mathbf{G}^t(\mathbf{r}, \mathbf{r}') = [\mathbf{n}'(\mathbf{r}') \times (\mathbf{r} - \mathbf{r}')]/[4\pi|\mathbf{r} - \mathbf{r}'|^3]. \quad (4.23)$$

At this point we should verify that we have achieved our desired goals. First, it is evident from (4.23) that $\mathbf{G}^t(\mathbf{r}, \mathbf{r}')$ is analytic in the components of \mathbf{r} for $\mathbf{r} \in V$ and $\mathbf{r}' \in S$.

Therefore, from the representation (4.22), we see that, under mild conditions on $\psi(\mathbf{r}')$, $\mathbf{A}^t(\mathbf{r})$ will be analytic in V . Second, it can be verified, for \mathbf{r} within V and $\mathbf{r}' \in S$, that \mathbf{G}^t has the properties

$$\nabla \cdot \mathbf{G}^t(\mathbf{r}, \mathbf{r}') = 0, \quad (4.24)$$

$$\nabla \times [\nabla \times \mathbf{G}^t(\mathbf{r}, \mathbf{r}')] = 0. \quad (4.25)$$

Note that these relations are analogous to the relations (4.17) and (4.18) for \mathbf{G}^n . It follows, by the same reasoning used in the case of \mathbf{G}^n and \mathbf{A}^n , that \mathbf{A}^t satisfies relations analogous to (4.19) and (4.20), and these relations hold exactly even in the presence of errors in the surface values $\psi(\mathbf{r}')$ and no matter how poorly the integrals (4.22) are evaluated. Similar to the case of \mathbf{G}^n , all that matters is that the kernel \mathbf{G}^t be evaluated to high precision.

4.1.4 Final Discussion

Let us put together what we have learned about analyticity and “exactness”. Look at (4.10) and (4.12). Since $\mathbf{A}^n(\mathbf{r})$ and $\mathbf{A}^t(\mathbf{r})$ are both analytic in V , $\mathbf{A}(\mathbf{r})$ will be analytic in V . Correspondingly, by (4.10), $\mathbf{B}(\mathbf{r})$ will be analytic in V . And since (4.17), (4.18), (4.24), and (4.25) hold, analogous results will hold for $\mathbf{A}(\mathbf{r})$,

$$\nabla \cdot [\mathbf{A}(\mathbf{r})] = 0, \quad (4.26)$$

$$\nabla \times [\nabla \times \mathbf{A}(\mathbf{r})] = 0. \quad (4.27)$$

Moreover, analyticity and the relations (4.26) and (4.27) will still hold exactly even in the presence of errors in the surface values B_n and ψ , and no matter how poorly the relevant integrals are evaluated. Finally, in view of (4.16), the Maxwell equation

$$\nabla \cdot \mathbf{B} = 0 \quad (4.28)$$

will be satisfied exactly. And, in view of (4.16) and (4.27), the second Maxwell equation

$$\nabla \times \mathbf{B} = 0 \quad (4.29)$$

will also be satisfied exactly.

We finally note, as a consequence of (4.26) and (4.27) and analogous relations for \mathbf{A}^n and \mathbf{A}^t , that there are the relations

$$\nabla^2 \mathbf{A} = \nabla^2 \mathbf{A}^n = \nabla^2 \mathbf{A}^t = 0. \quad (4.30)$$

All the Cartesian components of \mathbf{A} , \mathbf{A}^n , and \mathbf{A}^t are harmonic functions.

4.2 Procedure

We will now illustrate how the mathematical results of Subsection 4.1 can be applied. For simplicity, we will restrict our attention to the case of a dipole (which may be a combined-function dipole) and the use of the surface illustrated in Figure 4.

4.2.1 Selection of Hamiltonian and Scaled Variables

Even though the design orbit in a dipole is curved, it and the transfer map about it are usually most easily calculated using Cartesian coordinates with z as the independent variable. In this subsection we will describe the Hamiltonian for this purpose, first for unscaled variables and then for scaled dimensionless variables.

Selection of Hamiltonian

When z is taken to be the independent variable, the time t becomes a dependent variable and the Hamiltonian K for particle motion takes the form

$$K = -[p_t^2/c^2 - m^2c^2 - (p_x - qA_x)^2 - (p_y - qA_y)^2]^{1/2} - qA_z. \quad (4.31)$$

Here p_t is the canonical momentum conjugate to t .

Let β and γ be the usual relativistic factors defined by

$$\beta = v/c, \quad (4.32)$$

$$\gamma = (1 - \beta^2)^{-1/2}, \quad (4.33)$$

where v is the particle velocity. Then the magnitude of the mechanical momentum is given by the relation

$$p = \gamma mv = \gamma\beta mc, \quad (4.34)$$

and the quantity p_t has the value

$$p_t = -(m^2c^4 + p^2c^2)^{1/2} = -\gamma mc^2. \quad (4.35)$$

Since K is independent of t , the quantities p_t and p will be constants of motion. Finally, let p^0 be the momentum for the design orbit.

Scaled Dimensionless Variables

At this point it is useful to introduce dimensionless/scaled variables by the rules

$$\hat{x} = x/\ell, \quad (4.36)$$

$$\hat{y} = y/\ell, \quad (4.37)$$

$$\tau = ct/\ell, \quad (4.38)$$

$$\hat{p}_x = p_x/p^0, \quad (4.39)$$

$$\hat{p}_y = p_y/p^0, \quad (4.40)$$

$$p_\tau = p_t/(p^0 c). \quad (4.41)$$

Here ℓ is a convenient scale length.

The dimensionless variables satisfy the Poisson bracket rules

$$[\hat{x}, \hat{p}_x] = [\hat{y}, \hat{p}_y] = [\tau, p_\tau] = 1/(\ell p^0). \quad (4.42)$$

From now on we will redefine their Poisson brackets so that conjugate dimensionless variables have the usual unity Poisson brackets. This is permissible providing the Hamiltonian K is replaced by a properly scaled new Hamiltonian H given by the relation

$$\begin{aligned} H &= -[1/(\ell p^0)]\{[(p^0 c)^2 p_\tau^2/c^2 - m^2 c^2 - (p^0 \hat{p}_x - q A_x)^2 - (p^0)^2 \hat{p}_y^2]^{1/2} + q A_z\} \\ &= -(1/\ell)\{p_\tau^2 - (mc/p^0)^2 - (\hat{p}_x - \mathcal{A}_x)^2 - (\hat{p}_x - \mathcal{A}_x)^2\}^{1/2} + \mathcal{A}_z\} \end{aligned} \quad (4.43)$$

where

$$\mathcal{A}_x(\hat{x}, \hat{y}, z) = (q/p^0)A_x(\ell\hat{x}, \ell\hat{y}, z), \quad (4.44)$$

$$\mathcal{A}_y(\hat{x}, \hat{y}, z) = (q/p^0)A_y(\ell\hat{x}, \ell\hat{y}, z), \quad (4.45)$$

$$\mathcal{A}_z(\hat{x}, \hat{y}, z) = (q/p^0)A_z(\ell\hat{x}, \ell\hat{y}, z). \quad (4.46)$$

4.2.2 Interpolation and Evaluation of Integrals for \mathbf{A}

How are the various integrals appearing in Section 4.1 to be evaluated numerically? Carry out the following steps:

1. Suppose the surface S is subdivided into flat and curved portions in such a way that the flat portions (such as the surfaces of the straight end legs) consist of rectangles. Next map the curved portions (such as the top, bottom, and sides of the shaded portions of the surface in Figure 4) into rectangles.
2. Select *cubature* points on all these rectangles. Then map these points back into S to form a set of grid points on S , which we call *surface* grid points.
3. We assume there is also a three-dimensional *rectangular* grid, associated with the electromagnetic solver, on which the values of $\mathbf{B}(x, y, z)$ and $\psi(x, y, z)$ have been found by the solver. We again call this grid the *solver* grid. For each surface grid point interpolate $\mathbf{B}(x, y, z)$ and $\psi(x, y, z)$ values at nearby solver grid points, using for example cubic interpolation, to obtain associated surface grid-point values.

4. From the surface grid-point values \mathbf{B} construct associated values of B_n .
5. When required for any point $\mathbf{r} \in V$, obtain the values $\mathbf{A}^n(\mathbf{r})$ and $\mathbf{A}^t(\mathbf{r})$ by evaluating the integrals (4.14) and (4.22) using rectangular cubature formulas for all the rectangles of item 2 above. In the case of curved elements in S , take into account the Jacobian associated with mapping them into rectangles. If various derivatives of $\mathbf{A}(\mathbf{r})$ [and hence of $\mathbf{A}^n(\mathbf{r})$ and $\mathbf{A}^t(\mathbf{r})$] are required with respect to the components of \mathbf{r} , evaluate the associated derivatives of \mathbf{G}^n and \mathbf{G}^t analytically and use these results before employing the cubature formulas. That is, differentiate (4.14) and (4.22) under the integral sign.

4.2.3 Calculation of Design Orbit

The calculation of the design orbit typically involves a fitting process. Let z^{en} and z^{ex} denote the values of z at *entry* and *exit*. Then, for various values of the initial conditions, including p_τ , and for various dipole strengths, the equations of motion generated by H must be integrated over the interval $z \in [z^{\text{en}}, z^{\text{ex}}]$ until a suitable design orbit is found.⁷ Note that these differential equations will depend on \mathbf{A} and its first-order derivatives with respect to \hat{x} and \hat{y} . By *suitable* it is meant, for example, that the design orbit should pass through the good-field region of the dipole, have the desired bend angle, and have the desired entry and exit angles.

4.2.4 Calculation of Map

Introduce deviation variables about the design orbit and expand the Hamiltonian in these variables to find the homogeneous polynomials H_2, H_3, \dots . So doing will require homogeneous polynomial expansions (also about the design orbit) of $\mathbf{A}(\mathbf{r})$ [and hence of $\mathbf{A}^n(\mathbf{r})$ and $\mathbf{A}^t(\mathbf{r})$]. Produce these polynomial expansions by (analytically) making homogeneous polynomial expansions (again about the design orbit) of the kernels \mathbf{G}^n and \mathbf{G}^t before employing the cubature formulas. With these results in hand, numerically integrate the map equations of Subsection 1.7.2 to ultimately determine what we will call \mathcal{M}^{BB} , the map obtained using the *Bent Box* vector potential.

4.2.5 End-Field Terminations

Recall Figure 4. Suppose the straight end legs, which enclose the fringe-field regions, are long enough so that the magnetic field \mathbf{B} is sufficiently small at entry and upon exit. It is found, upon calculating \mathbf{A} with the use of (4.12), (4.14), and (4.22), that \mathbf{A} may still be sizable at the ends. In this case use of the end-field termination procedure described in Section 3.3 is essential.

⁷Sometimes it is more convenient to begin integrations at the center of the dipole and then work outwards.

Let $\mathcal{M}^{ben \rightarrow aex}$ be the symplectic map that relates the canonical coordinates (in Cartesian variables and in the Poincaré-Coulomb gauge) *after exit* to those *before entry*. Also, as in Subsection 3.3.4, let the two gauge transformations at *entry* and at *exit* be described by the symplectic maps \mathcal{M}^{en} and \mathcal{M}^{ex} . With the aid of these two maps, the full map $\mathcal{M}^{ben \rightarrow aex}$ describing the relation between the initial conditions just before entry and the final conditions just after exit can then be written in the form

$$\mathcal{M}^{ben \rightarrow aex} = \mathcal{M}^{en} \mathcal{M}^{BB} \mathcal{M}^{ex}. \quad (4.47)$$

4.2.6 Reference-Plane/Pole-Face Rotations

There is still one last step to be made. By design, a dipole produces a *bent* design orbit. When Cartesian variables/coordinates are used, the entry and exit reference planes are planes of constant z . We would like the incoming/entry reference plane to be normal to the incoming design orbit and the outgoing/exit reference plane to be normal to the outgoing design orbit. We will call these two reference planes the *standard* reference planes.

The relation between canonical coordinates with respect to planes of constant z and the standard reference planes can be described by two symplectic maps, denoted as \mathcal{M}^{proten} and \mathcal{M}^{protex} , which *rotate* the reference plane at *entry* and at *exit*. (Rotation of the reference plane is also sometimes referred to as *pole-face rotation*.) See, for example, Figure 5.

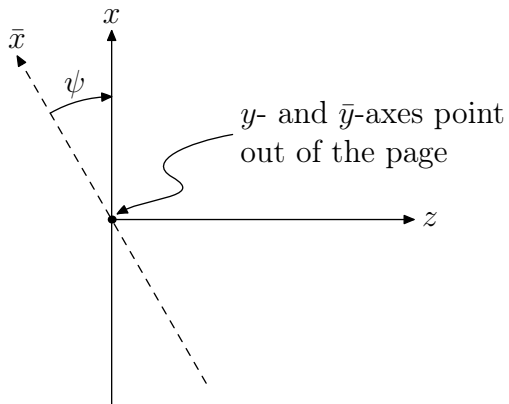


Figure 5: The map \mathcal{M}^{proten} describing the relation between the standard \bar{x}, \bar{y} entry/incoming reference plane and an x, y plane of constant z .

There is a well-defined procedure for computing these maps, including reference-plane rotation in the presence of a (perhaps residual) magnetic field. With the aid of these maps the net map \mathcal{M} that relates incoming and outgoing coordinates, with respect to the standard reference planes, is given by the product

$$\mathcal{M} = \mathcal{M}^{proten} \mathcal{M}^{ben \rightarrow aex} \mathcal{M}^{protex}. \quad (4.48)$$

Upon combining (4.47) and (4.48) we obtain the final product result

$$\mathcal{M} = \mathcal{M}^{proten} \mathcal{M}^{en} \mathcal{M}^{BB} \mathcal{M}^{ex} \mathcal{M}^{prote.x}. \quad (4.49)$$

4.3 Benchmarking and Smoothing Tests

Benchmarking

There are at least two ways to test/benchmark the accuracy of the procedures outlined in Section 4.2:

- (a) There are *magnetic charge* configurations for which both $\mathbf{B}(x, y, z)$ and $\psi(x, y, z)$ as well as an associated vector potential can be computed analytically. One of the simplest is that of a magnetic monopole doublet. [In that case the vector potential could be that for two magnetic monopoles of opposite sign with associated strings running to infinity. Call this vector potential $\mathbf{A}^{mmd}(x, y, z)$ to indicate that it is the vector potential of a *magnetic monopole doublet*.]

After selecting a spacing between the monopoles in the doublet and a design energy, a design orbit can be integrated through the \mathbf{B} field in such a way that it lies in a plane perpendicular to the straight line joining the monopoles and passes directly between the poles of the monopole doublet. Subsequently, the strength of the monopoles in the doublet could be adjusted to achieve some desired bend angle. Finally, with a design orbit in hand, one could set up a surrounding bent box with legs.

Now that the parameters for the monopole doublet have been specified, set up a rectangular three-dimensional grid (say with equal spacings in all three Cartesian coordinates) and compute the values of $\mathbf{B}^{sv}(x, y, z)$ and $\psi^{sv}(x, y, z)$ at the grid points. Here we have introduced the superscript *sv* because we wish to view these values as *solver values*.

Since the parameters for the bent box with legs have also been specified, and thereby the surface S , set up a surface grid as described in steps 1 and 2 in Subsection 4.2.1. Execute steps 3 and 4 in Subsection 4.2.1 to obtain a set of B_n and ψ values on the surface grid points

Execute step 5 in Subsection 4.2.1 to obtain $\mathbf{A}^{bbv}(x, y, z)$ and its derivatives at any desired point interior to S . Here we have introduced the superscript *bbv* to emphasize that *bent-box values* are being used.

At the interior solver grid points compute $\mathbf{B}^{bbv}(x, y, z)$ using $\mathbf{A}^{bbv}(x, y, z)$ in (3.43). Compare $\mathbf{B}^{bbv}(x, y, z)$ evaluated at the interior solver grid points with the solver values for $\mathbf{B}^{sv}(x, y, z)$ at these points. [Note that most interior values of $\mathbf{B}(x, y, z)$ and $\psi(x, y, z)$ played no role in the calculation of $\mathbf{A}^{bbv}(x, y, z)$ since interpolation onto the surface grid involved only solver points very close to the surface grid points.] Provided

the solver and surface grids are sufficiently fine, when this comparison is made excellent agreement through many significant figures is found between interior solver grid-point values of \mathbf{B}^{bbv} and \mathbf{B}^{sv} .

The benchmark test so far has compared magnetic fields. One can extend this test to also compare *maps*. Let \mathcal{M}^{exact} be the *exact* map computed using the magnetic monopole doublet vector potential $\mathbf{A}^{mmd}(x, y, z)$ and let \mathcal{M}^{bbv} be the map computed using the vector potential $\mathbf{A}^{bbv}(x, y, z)$. In general these maps will differ because, while $\mathbf{A}^{mmd}(x, y, z)$ and $\mathbf{A}^{bbv}(x, y, z)$ produce essentially the same magnetic field as described above, they differ by a gauge transformation. However, suppose both these maps are transformed, analogous to what was done in (4.47), to bring them to maps for which the initial and final vector potentials are in the Poincaré-Coulomb gauge. When this is done, excellent agreement is found between the two transformed maps.

- (b) Use a field solver to find the fields $\mathbf{B}^{sv}(x, y, z)$ and $\psi^{sv}(x, y, z)$ on some solver grid for some curved beam-line element of interest. Following the steps outlined in item (a) above, compute $\mathbf{A}^{bbv}(x, y, z)$ and its first derivatives at any interior point. From these first derivatives compute $\mathbf{B}^{bbv}(x, y, z)$ at any interior point using (3.43). Compare interior solver grid-point values of \mathbf{B}^{bbv} and \mathbf{B}^{sv} . This comparison also tests how “Maxwellian” the $\mathbf{B}^{sv}(x, y, z)$ solver values actually are. Provided the solver and surface grids are sufficiently fine, when this comparison is made excellent agreement through many significant figures is found between interior solver grid-point values of \mathbf{B}^{bbv} and \mathbf{B}^{sv} .

Note that when simply comparing fields, it is not really necessary to set up a design orbit and select a corresponding bent box with straight end legs. The use of any box, bent or straight, can be tested as long as the box fits within the solver grid and its ends are long enough to extend into essentially field-free regions.

Smoothing Tests

Note that, according to (4.30), the components of $\mathbf{A}(x, y, z)$ are guaranteed to be harmonic functions. Let $\mathbf{A}^{true}(x, y, z)$ be the result of evaluating the surface integrals (4.14) and (4.22) using very careful integration and high-quality field data. Also, let $\mathbf{A}^{approx}(x, y, z)$ be the result of evaluating the surface integrals (4.14) and (4.22) in some *approximate* fashion and employing only *approximately* accurate field data. The difference between these two results is a measure of the *error* produced as a result of these approximations,

$$\mathbf{A}^{error}(x, y, z) = \mathbf{A}^{approx}(x, y, z) - \mathbf{A}^{true}(x, y, z). \quad (4.50)$$

Since the difference of two harmonic functions is again a harmonic function, the components of $\mathbf{A}^{error}(x, y, z)$ will be harmonic functions. Moreover, since harmonic functions take their extrema on boundaries, we expect that the magnitude of $\mathbf{A}^{error}(x, y, z)$ will decrease with distance from S .

To see how this expectation is realized in practice, there are at least two ways to test how sensitive surface methods are to noise in the field values at solver grid points:

- Use a field solver to find the fields on some solver grid for some beam-line element of interest. Following the steps outlined in item (a) above, compute $\mathbf{A}^{bbv}(x, y, z)$ and its derivatives through some fixed order at any interior point. To model the effect of noise, modify the fields at the solver grid points in some small and random way. For example, at each solver grid point one might make the replacements

$$\mathbf{B}(x, y, z) \rightarrow \mathbf{B}(x, y, z) + |\mathbf{B}(x, y, z)|\epsilon_B(x, y, z)\mathbf{n}(x, y, z), \quad (4.51)$$

$$\psi(x, y, z) \rightarrow \psi(x, y, z) + \epsilon_\psi(x, y, z)\psi(x, y, z). \quad (4.52)$$

Here the $\mathbf{n}(x, y, z)$ are unit vectors to be chosen randomly at each solver grid point, and at each solver grid point $\epsilon_B(x, y, z)$ and $\epsilon_\psi(x, y, z)$ are to be chosen randomly from small intervals, say $\epsilon_B(x, y, z) \in [-.01, .01]$ and $\epsilon_\psi(x, y, z) \in [-.01, .01]$. Use the modified fields to find associated modified $\mathbf{A}^{bbv}(x, y, z)$ and its derivatives. Repeat this operation for several random number seeds. Examine how the so generated ensemble of modified $\mathbf{A}^{bbv}(x, y, z)$ and its derivatives compares to the $\mathbf{A}^{bbv}(x, y, z)$ and its derivatives computed in the absence of noise. If desired, compute also the associated maps \mathcal{M} , including end-field termination effects following (4.47), and examine how they compare.

- Examine how sensitive the $\mathbf{A}^{bbv}(x, y, z)$ values and their derivatives through some fixed order at any interior point, and the associated interior \mathbf{B} values given by (4.10), are to the values of $\mathbf{B}(x, y, z)$ and $\psi(x, y, z)$ at any given solver grid point. Do this by setting all solver grid point field values to zero save for one, for which \mathbf{B} is taken to be a randomly chosen unit vector and for which, say, $\psi = \pm 1$. Let z^* be the value of z for the solver grid point at which the field is taken to be nonzero. It is expected that the contribution of any solver grid point field value should fall off with distance from the location of the solver grid point. For this reason, arrange to have $z^* \approx 0$. (Here we assume that the coordinate system has been chosen so that the beam-line element under study is centered about $z = 0$.)

5 Closing Summary

We have described the use of surface methods for both straight and curved beam-line elements, and the use of the minimum gauge at element ends. These surface methods begin with three-dimensional field data on a grid provided by some magnetic field solver, and result in a design orbit and the symplectic transfer map about that orbit. The Maxwell equations are satisfied exactly and analyticity is assured. We have also described how these methods, because they exploit the properties of harmonic functions, are expected

to be relatively insensitive to numerical noise, and we have described methods for testing this expectation. Based on these methods, it is now possible for the first time to compute realistic symplectic transfer maps to high order including all multipole-error and fringe-field effects. These maps can then be used to realistically predict/evaluate the expected performance of both linear and circular machines.

Bibliography

1. A. Dragt, *Lie Methods for Nonlinear Dynamics with Applications to Accelerator Physics* (2016), available on the Web at
<http://www.physics.umd.edu/dsat/dsatliemethods.html>
2. M. Venturini and A. Dragt, “Accurate Computation of Transfer Maps from Magnetic Field Data”, *Nuclear Instruments and Methods* **A427**, p. 387 (1991).
3. C. Mitchell and A. Dragt, “Accurate transfer maps for realistic beam-line elements: Straight elements”, *Physical Review Special Topics - Accelerators and Beams* **13** 064001 (2010).
4. C. Mitchell, *Calculation of Realistic Charged-Particle Transfer Maps*, University of Maryland Physics Department Ph.D. thesis (2007), available on the Web at
<http://www.physics.umd.edu/dsat/>
5. É. Forest, *Beam Dynamics: A New Attitude and Framework*, Harwood Academic Publishers (1998).